Nanoscale Advances

REVIEW

View Article Online
View Journal | View Issue

Cite this: *Nanoscale Adv.*, 2023, **5**, 2846

Synthesis of F-doped materials and applications in catalysis and rechargeable batteries

Jiale Huo, [ab] Yaofang Zhang,*[ab] Weimin Kang, [ac] Yan Shen,[ab] Xiang Li,[ab] Zirui Yan,[ab] Yingwen Pan[ab] and Wei Sun [ab]

Received 28th February 2023
Accepted 27th April 2023

DOI: 10.1039/d3na00126a

rsc.li/nanoscale-advances

Elemental doping is one of the most essential techniques for material modification. It is well known that fluorine is considered to be a highly efficient and inexpensive dopant in the field of materials. Fluorine is one of the most reactive elements with the highest electronegativity ($\chi = 3.98$). Compared to cationic doping, anionic doping is another valuable method for improving the properties of materials. Many materials have physicochemical limitations that affect their practical application in the field of catalysis and rechargeable ion batteries. Many researchers have demonstrated that F-doping can significantly improve the performance of materials for practical applications. This paper reviews the applications of various F-doped materials in photocatalysis, electrocatalysis, lithium-ion batteries, and sodium-ion batteries, as well as briefly introducing their preparation methods and mechanisms to provide researchers with more ideas and options for material modification.

1 Introduction

Since the 21st century, environmental issues have become the primary problems hindering sustainable development. Over the past 20 years, many methods have been used to remove toxic pollutants, such as coagulation, membrane treatment, adsorption, ion exchange, and photocatalysis.[1–3] Since Fujishima and Honda first demonstrated photocatalytic hydrolysis at TiO_2 electrodes under UV light in 1972,[4] catalytic technology has been applied in various fields to solve the increasingly serious environmental pollution problems. At present, semiconductor photocatalysis is attracting much attention from researchers because of its promising applications in degrading organic pollutants to clean up air and water pollution. The principle of photocatalysis is based on the redox ability of photocatalysts in the presence of light to degrade pollutants.[5] Photocatalysis, although varying in detail in terms of reactions and mechanisms, can be described in terms of four crucial steps (as shown in Fig. 1a): (I) absorption of light to generate electron–hole pairs; (II) separation of the excitation charge; (III) transfer of electrons and holes to the surface of the photocatalyst; and (IV) redox reactions using the charge on the surface. Some organic pollutants such as phenol,[6–8] toluene,[9–11] methyl orange,[12] methylene blue,[13,14] rhodamine B,[15,16] diclofenac,[17–19] atrazine,[20,21] and perfluorooctanoic acid[22,23] enter the atmosphere and water bodies, seriously endangering environmental safety and threatening the health of living organisms. Common photocatalysts such as titanium dioxide, zinc oxide, tin oxide, zirconium dioxide, and cadmium sulfide have shown good photocatalytic performance.[24]

Developing sustainable, environmentally friendly pathways to produce globally significant fuels and chemicals can play an important role in reducing carbon emissions while providing the raw materials necessary for human survival.[25–27] One promising goal is to use electrochemical conversion processes to convert atmospheric molecules (such as water, carbon dioxide, and nitrogen) into higher-value products (such as hydrogen, hydrocarbons, oxygenates, and ammonia) by combining them with renewable energy sources (Fig. 1b).[28] Electrocatalysts play a key role in these energy conversion technologies as they increase the rate, efficiency, and selectivity of the chemical conversions involved. However, conventional electrocatalysts are not sufficient. The greatest challenge is to develop advanced electrocatalysts and improve their performance to achieve widespread access to clean energy technologies. Electrocatalysis is a catalytic action that causes charge transfer at the electrode and electrolyte interface to accelerate a reaction. Electrocatalysis is widely used for the electrolytic reduction of carbon dioxide[29–31] and nitrogen,[32–35] organic degradation,[36] hydrogen evolution reaction,[37] and oxygen reduction reactions.[38] The rational selection of electrode materials is of great importance for the economical and efficient operation of electrodes. Excellent electrode materials should not only be effective in degrading pollutants, but also have stable electrochemical properties and be inexpensive.

[a]State Key Laboratory of Separation Membranes and Membrane Processes, Tiangong University, Tianjin 300387, PR China. E-mail: zhangyaofang@tiangong.edu.cn
[b]School of Physical Science and Technology, Tiangong University, Tianjin 300387, PR China
[c]School of Textile Science and Engineering, Tiangong University, Tianjin 300387, China

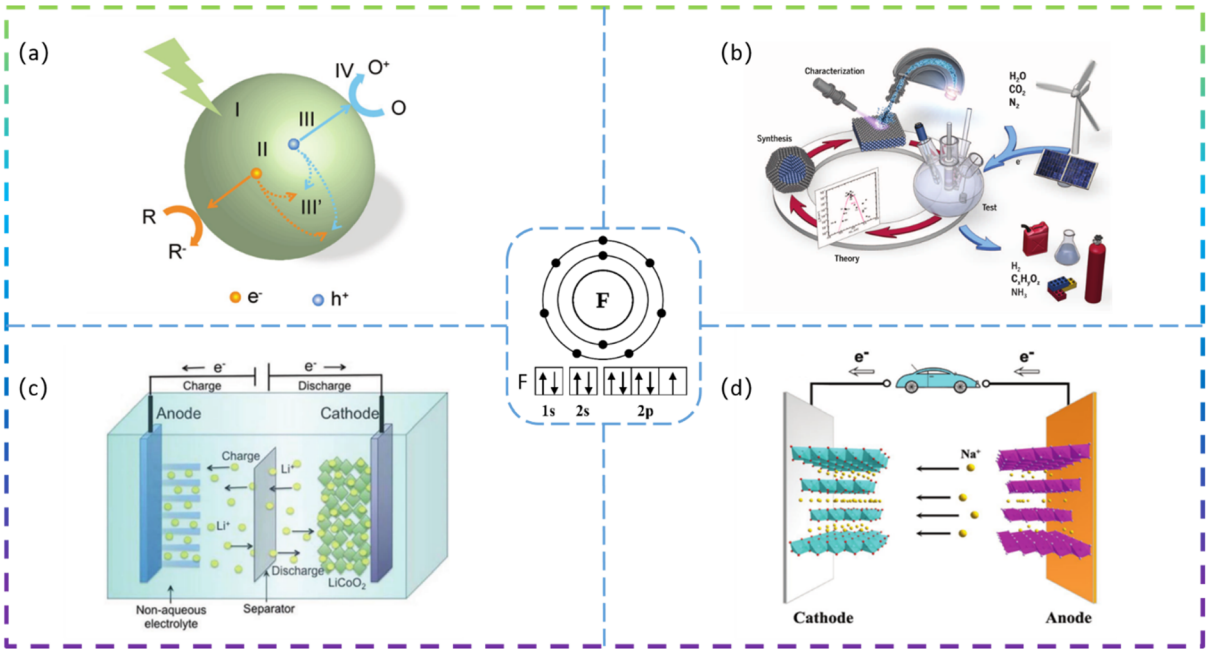

Fig. 1 (a) Steps in the photocatalytic reaction process. (b) Schematic showing electrochemical conversion of water, carbon dioxide, and nitrogen into value-added products (*e.g.*, hydrogen, hydrocarbons, oxygenates, and ammonia), using energy from renewable sources. (c) Schematic diagram of the lithium intercalation–deintercalation reaction mechanism in a rechargeable lithium-ion battery. (d) Schematic illustration of SIBs (the inset shows the electron configuration of the F atom).

Lithium-ion batteries (LIBs) have received a lot of attention because of their high energy density, high power density, long cycle life, and low memory effect.[39] LIBs have been under development as a power source for portable electronic devices, electric vehicles, and energy storage systems. The development of next-generation LIBs with high energy/power density and long life is now necessary to address the rapidly growing energy demand in our daily lives. Typically, LIBs consist mainly of a positive electrode, a negative electrode, a separator, and a liquid electrolyte (Fig. 1c).[40] The electrode material is the key to developing high-energy, high-power density lithium-ion batteries. In recent years, sodium-ion batteries (SIBs) have attracted extensive research attention due to their abundant and cheap sodium resources. A schematic diagram of the operating principle of a sodium ion battery is shown in Fig. 1d.[41]

Researchers modify materials to achieve more outstanding properties through various techniques such as doping, coating, controlling the structure of the material, and pre-treatment. Among the various dopants, fluorine is a very common and efficient dopant because of its abundant and cheap source. It is well known that F-doped materials have a wide range of applications, and we have searched the Web of Science for articles on F-doped material applications over the last decade and found that they are highly represented in photocatalytic, electrocatalytic, LIB and SIB applications. Fig. 2 summarises the number of SCI papers published on F-doped materials in photocatalysis, electrocatalysis, and batteries in the last decade (up to September 2022). It is clear that F-doped materials are receiving increasing attention in these applications.

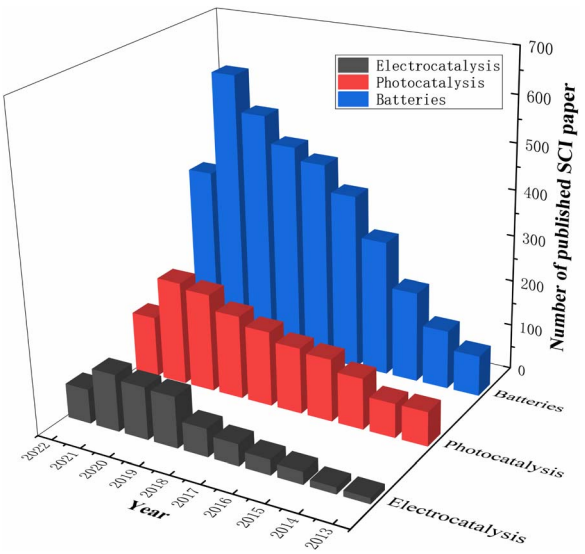

Fig. 2 Statistics of F-doped materials' core publications in photocatalysis, electrocatalysis and batteries.

2 Applications and synthetic strategies for F-doped materials in catalysis

2.1 Photocatalysis

2.1.1 Degradation of phenol. Phenol is an organic chemical that is harmful to the environment and can cause pollution to water bodies and the atmosphere. In addition, phenol has

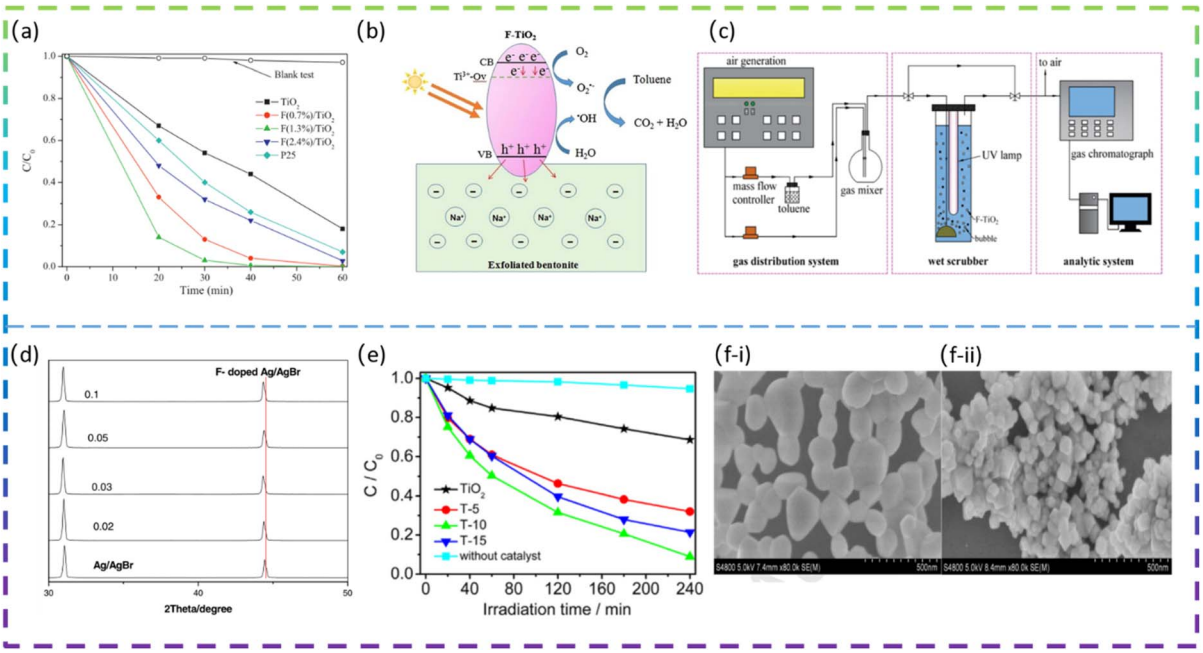

Fig. 3 (a) Concentration changes of the phenol as a function of light irradiation time. (b) Proposed mechanism for the photocatalytic degradation of toluene on the TF5-400/EB composite. (c) Schematic of the experimental setup. (d) Partially enlarged XRD patterns of undoped and F-doped Ag/AgBr. (e) Photocatalytic degradation of methylene blue by TiO_2, T-5, T-10, and T-15 under visible light irradiation. SEM images of the as-prepared CeO_2 nanoparticles (f-i) and F(1/3)-CeO_2 nanoparticles (f-ii).

a strong corrosive effect on the skin and mucous membranes and can damage the central nervous system or inhibit liver and kidney function.[6–8,42,43]

Yu *et al.* fabricated square-shaped TiO_2 nanocrystals doped with different F contents *via* the sonochemical method. The doping of the optimal content of F (1.3 mol%) gives a 5.3 times increase in the phenol degradation rate (Fig. 3a). The high photocatalytic degradation activity of the doped TiO_2 is due to the factor that the F doping increases the number of hydroxyl groups on the TiO_2 surface, which effectively reduces the recombination rate of photogenerated electron/hole pairs and thus generates more ·OH radicals to decompose phenol molecules.[44]

2.1.2 Degradation of VOCs. Volatile organic compounds (VOCs) are important air pollutants and pose a threat to human health.[45] Toluene, ethylene, xylene, formaldehyde, acetaldehyde, ethyl acetate, and methylene chloride are the most typical components of VOCs in the environment.[9,46]

Wang *et al.* prepared an F-doped TiO_2/exfoliated bentonite (TF/EB) composite by dispersing F-doped TiO_2 (TF) nanoparticles on an exfoliated bentonite (EB) using a facile sol–gel method. The presence of F^- ions increases the percentage of exposed reactive facets on TiO_2. In addition, F^- ions doped in the TiO_2 lattice create oxygen vacancies and Ti^{3+} defects, which affect the transfer and migration of photocatalytic carriers and induce visible light photocatalytic activity. Fig. 3b shows the proposed mechanism for the improved photocatalytic performance of the TF5-400/EB (F/Ti atomic ratio was 5% and calcination was done at 400 °C) photocatalyst.[10] Xie *et al.* synthesized F-doped TiO_2 and employed it in wet-scrubbing coupled with the photocatalytic oxidation (WPCO) process. The experimental setup is shown in Fig. 3c. Toluene removal efficiency reached 80% over F-TiO_2, while it was only 25% over TiO_2 in the WPCO process. In addition, its corresponding mineralization capacity is significantly higher, with CO_2 from the oxidation of toluene in the coupling reaction being approximately 92 ppmv. The F-doping produces more mobile ·OH, which is responsible for the excellent toluene degradation and mineralization photocatalytic activity.[11]

2.1.3 Degradation of methyl orange. Increasing water pollution with the development of the dye industry has inspired researchers to develop efficient and stable visible-light-driven photocatalysts. Bao *et al.* synthesized novel F-doped Ag/AgBr photocatalysts containing various amounts of F^- by an ion exchange method and exhibited excellent photocatalytic performance for methyl orange degradation. Powder X-ray diffraction (XRD) results show that F^- is inserted into the lattice of AgBr (Fig. 3d), partially replacing Br^- and causing AgBr lattice contraction. The photocatalytic activity of F-doped Ag/AgBr is significantly dependent on the amount of F^-. The results indicated that the main active substance in the degradation of methyl orange was ·OH. The main enhancement mechanism was the inhibition of the recombination of the electron–hole pairs by F^-.[12]

2.1.4 Degradation of methylene blue. Methylene blue dyes have many potential applications in the textile, paper, dyeing, printing, coating, pharmaceutical, and food industries.[14] However, methylene blue is highly toxic and carcinogenic to organisms.[13] Therefore, the removal of methylene blue from wastewater cannot be ignored.

Yu *et al.* successfully synthesized F-doped TiO_2 (F-TiO_2) using a modified sol–gel method. The results showed that the photocatalytic degradation of methylene blue by F-TiO_2 was enhanced, with a maximum degradation rate of 91% for F-TiO_2 and 32% for pure TiO_2 under visible light irradiation. The doping of F in TiO_2 increases the absorption of visible light, promotes the separation of photogenerated electrons and holes, and enhances the photocatalytic oxide species; the doping of F also leads to enhanced surface acidity and promotes the adsorption of reactant molecules, thus improving the photocatalytic activity of TiO_2.[47] Miao *et al.* synthesized pure CeO_2 and fluorine-doped CeO_2 (F-doped CeO_2) using a low-temperature solution combustion method and subsequent heat treatment in air. The prepared samples doped with different nominal mass ratios of sodium fluoride were denoted as F(x)-CeO_2, where x is 1/10, 3/10, 1/3, and 2/5, respectively. It is found that F-doping makes the CeO_2 nanoparticles smaller in size and the CeO_2 nanocubes formed exposed a higher proportion of the reaction surface. The SEM images of pure CeO_2 and F-doped CeO_2 are shown in Fig. 3f-i and f-ii. It can be clearly seen that pure CeO_2 (Fig. 3f-i) has an irregular spherical morphology with an average diameter of about 100 nm, with some of the particles agglomerated into larger ones. In contrast, F(1/3)-CeO_2 (Fig. 3f-ii) has a size of about 50 nm. The band gap is estimated to be 3.16 eV and 2.88 eV, for pure CeO_2 and F-doped CeO_2 nanocubes, respectively. Interestingly, the F-doped CeO_2 nanoparticles exhibited excellent photocatalytic activity for the degradation of organic pollutants under UV and visible light irradiation. The apparent reaction rate constant k for methylene blue decomposition on the optimized F-doped CeO_2 nanocubes is 9.5 times higher than that on pure CeO_2 and 2.2 times higher than that on commercial TiO_2, respectively.[48]

2.1.5 Degradation of diclofenac. Diclofenac (DCF), a non-steroidal anti-inflammatory drug, has become a contaminant of concern.[17] Increased exposure to DCF not only causes health problems for aquatic organisms and higher plants but also poses a serious threat to mammals.[18,19]

Rueda-Salaya *et al.* prepared zinc oxide catalysts doped with different amounts of fluoride by the sol–gel technique. Compared to undoped ZnO, F-doped ZnO has better photocatalytic performance for DCF mineralization under simulated solar radiation conditions. The DCF of fluorine-doped ZnO degradation in solar radiation is shown in Fig. 4a. Under the optimized experimental conditions (1 g L^{-1} ZnO-F20 (ZnO semiconductor modified by the incorporation of 10 wt% fluorine) catalyst, DCF solution pH maintained at 6.5), the DCF was completely degraded, the chloride ions were completely released and the energy accumulated during drug degradation was 400 kJ m^{-2} with a mineralization rate of about 90%. The results show that as the amount of fluoride-doping increases, the crystal size decreases, the band gap value decreases slightly, and the specific surface area increases. F^- substituent addition to the ZnO network reduces the rate of complexation of e^-/h^+ pairs and improves photocatalytic activity under simulated solar irradiation.[49] Vitiello *et al.* synthesized fluorine-doped ZnO nano- and meso-crystals by a hydrothermal approach and investigated the following F atomic concentrations: 0 at% (bare, ZnO:F0), 0.25 at% (ZnO:F0.25), 0.5 at% (ZnO:F0.5) and 1 at% (ZnO:F1). Surprisingly, the sample with the lowest fluorine content (ZnO:F0.25) had the best photocatalytic efficiency. As the amount of F doping increases, there is a tendency for the defect concentration to increase. It is argued that the excess dopant increases the extent of defects in the ZnO crystal structure and becomes recombination centers for photogenerated carriers, leading to the deterioration of photocatalytic activity.

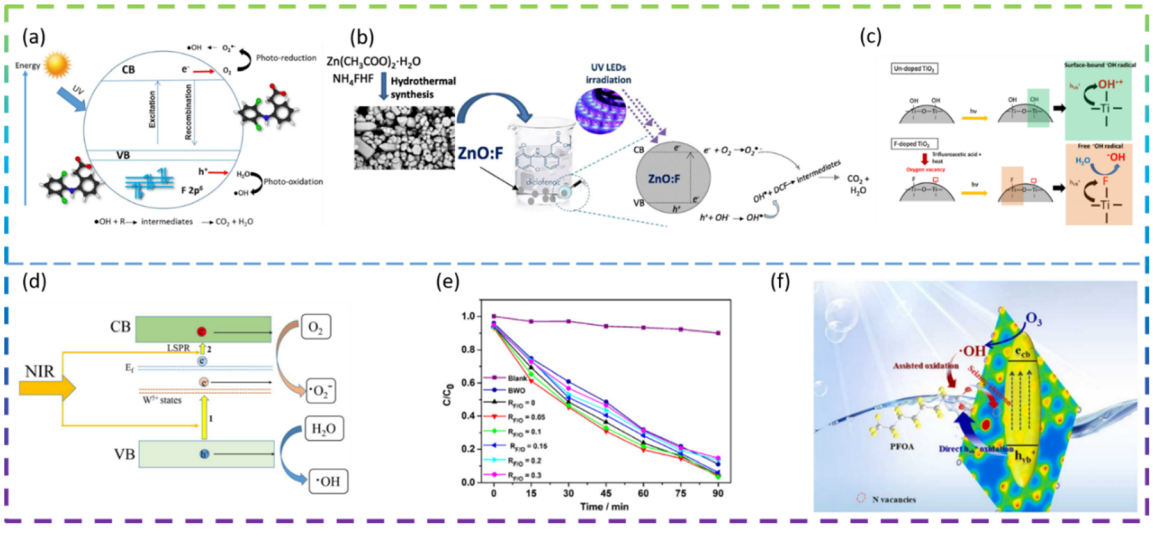

Fig. 4 (a) Schematic representation of DCF degradation using fluorine-doped zinc oxide under solar irradiation. (b) ZnO:F synthesis method and photocatalytic degradation mechanism of DCF. (c) Schematic diagram showing formation of surface-bound and free hydroxyl radicals on TiO_2. (d) Schematic illustration of the NIR photocatalytic mechanism of F-doped $(NH_4)_{0.33}WO_3$. (e) Photocatalytic degradation of RhB solution by BWO and the F-doped rGO-BWO samples with different RF/O values under visible light ($\lambda > 400$ nm) illumination. (f) Schematic diagram of F-doped g-C_3N_4 photocatalytic degradation of PFOA.

In fact, the introduction of F^- ions into the ZnO lattice can increase the concentration of free electrons in the conduction band and increase the n-type characteristics of the sample. ZnO:F0.25 has a higher hydrophilicity, which means a higher rate of hydroxyl radical production under UV irradiation. All doped samples exhibited high rates of DCF degradation and mineralization, mainly due to their high efficiency in generating hydroxyl radicals (·OH). The ZnO:F synthesis method and the mechanism of photocatalytic degradation of DCF are shown in Fig. 4b.[50]

2.1.6 Degradation of atrazine. Atrazine is widely used in agricultural production as a herbicide. However, long-term exposure to atrazine has amplified environmental and health risks worldwide.[20,21]

Samsudin *et al.* prepared mesoporous nanocrystalline F-doped TiO_2 for the photocatalytic degradation of atrazine using trifluoroacetic acid (TFA) as a fluorine precursor using a modified sol–gel method. The photocatalytic activity of F-doped TiO_2 is enhanced under UV light irradiation compared to undoped TiO_2. The F-doped TiO_2 also exhibits visible photocatalytic activity, which is due to the exogenous light absorption triggered by the oxygen vacancies and Ti^{3+}. The excellent photocatalytic activity under UV irradiation is due to the effective electron and hole separation and the enhanced absorption intensity in the UV region. In addition, upon photoexcitation, free radicals are generated on the surface of F-doped TiO_2, while less reactive hydroxyl radicals are generated on the surface of undoped TiO_2 (Fig. 4c). The higher fluorine doping in TiO_2 does not necessarily control the enhanced photocatalytic activity due to the excess oxygen vacancies acting as carrier traps. This suggests that an optimum doping condition exists for F-doped TiO_2 to maximize photocatalytic activity.[51]

2.1.7 Degradation of rhodamine B. Rhodamine B (RhB) is a positively charged dye that has been widely developed in the coatings, textile, plastics, paper, and printing industries. However, RhB is a recognized toxic pollutant and has been reported to exhibit carcinogenic and mutagenic effects in living systems.[15,16]

Kang *et al.* synthesized F-doped $(NH_4)_{0.33}WO_3$ as a novel near-infrared (NIR) photocatalyst. The NIR degradation of RhB by F-doped $(NH_4)_{0.33}WO_3$ was 83% within 180 min. The best F-doped $(NH_4)_{0.33}WO_3$ showed a NIR degradation rate of 0.0102 min^{-1} for RhB, which is about 8.5 times higher than that of $(NH_4)_{0.33}WO_3$. The enhanced NIR photocatalytic performance of F-doped $(NH_4)_{0.33}WO_3$ can be attributed to the remarkably enhanced generation and separation of NIR localized surface plasmon resonance (LSPR) induced electron–hole pairs (Fig. 4d).[52] Yu *et al.* synthesized reduced graphene oxide-Bi_2WO_6 (rGO-BWO) photocatalysts with the different $R_{F/O}$ values (molar ratio of the F molar mass and the O molar mass of Bi_2WO_6) *via* a one-step hydrothermal method. The photocatalytic activity of the F-doped rGO-BWO with $R_{F/O} = 0.05$ was superior to that of rGO-BWO and other F-doped rGO-BWO under 500 W Xe lamp irradiation. F^--ion doping enhances surface acidity, generates oxygen vacancies, increases active centers, and effectively inhibits electron–hole pair complexation through the rapid migration of photogenerated carriers.[53]

2.1.8 Degradation of perfluorooctanoic acid. Perfluorooctanoic acid (PFOA) is a typical perfluorinated compound that is widely detected in the environment due to its widespread use. PFOA is persistent and difficult to degrade, and when absorbed by the body it accumulates in the body, interfering with endocrine secretion and affecting normal metabolism and reproduction.[22,23]

Chen *et al.* regulated N vacancies, hydrophobic sites, and the electron-rich zone by doping F into g-C_3N_4 (CN) to accelerate photocatalytic ozonation of PFOA. F-CN activity was better than CN activity, with F-CN/Vis/O_3 removal of PFOA at 74.3% and CN/Vis/O_3 removal of PFOA at only 57.1%. The doping of F narrows the E_g of F-CN and shifts the VB potential downwards, which facilitates the generation of more E_{cb}^- (photogenerated electron)–H_{vb}^+ (photogenerated hole) and improves the oxidation of H_{vb}^+. In addition, the doping of F leads to more N vacancies on F-CN, which facilitates the H_{vb}^+ oxidation of PFOA. Hydrophobic sites and electron-rich regions induced by F atoms can facilitate the mass transfer of O_3 and PFOA, promote the reaction of O_3 with E_{cb}^- and inhibit the binding of E_{cb}^-–H_{vb}^+. The schematic diagram of the F-doped g-C_3N_4 photocatalytic degradation of PFOA is shown in Fig. 4f.[54]

2.1.9 Doping with other halogen elements. In recent years, the doping of halogen elements into photocatalysts has proven to be an effective method for modulating the band gap of photocatalysts. Non-metallic halogens are very attractive because of their high thermal stability and photosensitivity. For example, Phuruangrat *et al.* synthesized Cl-doped Bi_2MoO_6 as a visible light driven photocatalyst by a hydrothermal method. The photodegradation of RhB under visible light irradiation was 96.5%, 97.3%, and 99.5% for pure Bi_2MoO_6, Bi_2MoO_6 doped with 1 wt% Cl and Bi_2MoO_6 doped with 3 wt% Cl, within 160 min, respectively. It should be noticed that the photocatalytic performance of Cl-doped Bi_2MoO_6 was not significantly improved, but these results still demonstrate that Cl doping can play a photocatalytic role in the degradation of RhB under visible light irradiation, as Cl doping facilitates carrier transfer and reduces the recombination of photogenerated electron–hole pairs in Bi_2MoO_6.[55]

Zhang *et al.* prepared Br-doped $Bi_2O_2CO_3$ nanosheets *via* a one-step hydrothermal reaction. Under simulated solar irradiation, the sample with a trace Br content of 1.17 wt% showed the highest degradation efficiency for RhB, with a rate constant k that was 3.6 times higher than that of pure $Bi_2O_2CO_3$. According to crystal structure and Density Functional Theory (DFT) calculations, the interstitial doping of Br from cetyltrimethylammonium bromide (CTAB) into the $Bi_2O_2CO_3$ lattice as a dopant changes the band gap position of $Bi_2O_2CO_3$, generating delocalized impurity states at the Fermi energy level. The improved electronic structure gives Br-doped $Bi_2O_2CO_3$ a broader light-harvesting and accelerated charge migration.[56]

Zai *et al.* prepared rose-like I-doped $Bi_2O_2CO_3$ microspheres *via* a hydrothermal process. Under visible light ($\lambda > 400$ nm), RhB is completely degraded within 6 min and about 90% of Cr(VI) is reduced after 25 min. According to the crystal structure

of $Bi_2O_2CO_3$ and DFT calculations, I^- can partially replace CO_3^{2-} in $Bi_2O_2CO_3$, narrowing its band gap and enhancing its visible light absorption.[57]

2.1.10 Doping with non-metallic elements. Metal doping can optimize the performance of materials, but the disadvantages of metal dissolution and high cost have prevented the technique from being promoted. Therefore, doping of non-metallic elements into photocatalysts has been increasingly recognized as a viable strategy for improving photocatalytic performance due to its particular advantages in creating more active sites and accelerating carrier separation and transport. Liu *et al.* fabricated N-doped TiO_2 nanowire/N-doped graphene (N-TiO_2/NG) heterojunctions by a simple hydrothermal method. Compared to TiO_2 nanowire/graphene and N-doped TiO_2 nanowire/graphene composites, the N-TiO_2/NG heterostructures demonstrated better photocatalytic performance for the degradation of methylene blue under visible light irradiation and exhibited better recyclability. The results show that N-doping broadens the visible light absorption region of TiO_2, while N-doped graphene also improves the separation and transport of photogenerated electron–hole pairs and generates higher photocurrents, playing a crucial role in enhancing photocatalytic activity.[58]

Ding *et al.* designed P-doped $CeVO_4$ nanobelts by electrospinning process. In consecutive levofloxacin photocatalytic experiments, the P-doped $CeVO_4$ isomeric nanoribbons exhibited excellent photocatalytic activity, high long-term stability, and excellent reusability. The partial phase transition from tetragonal zircon (t-$CeVO_4$) to monoclinic monazite (m-$CeVO_4$) was induced by P-doping, and such a homogeneous junction resulted in a fully optimized t-$CeVO_4$/m-$CeVO_4$ interface with enhanced visible light capture and electron–hole transfer separation, contributing to effective visible light-induced photocatalysis.[59]

Table 1 Synthesis and photocatalytic properties of F-doped materials/other element-doped materials

No.	Materials	Preparation	Fluorine source/other doping element sources	Object	Light source	Photocatalytic efficiency	Ref.
1	F-doped TiO_2	Sonochemical method	NH_4F	0.050 g L^{-1} phenol	365 nm UV lamp	90% in 60 min	44
2	F-doped TiO_2/exfoliated bentonite	Sol–gel method	NH_4F	2000 ppb toluene	UV	71.6% in 80 min	10
3	F-doped TiO_2	One-step hydrothermal method	NH_2HF_2	30 ppmv toluene	UV	80% in 120 min	11
4	F-doped Ag/AgBr	Ion exchange method	NaF	20 mg L^{-1} methyl orange	Visible-light	91.9% in 12 min	12
5	F-doped TiO_2	Modified sol–gel method	NH_4F	10 mg L^{-1} methylene blue	Visible-light	91% in 240 min	47
6	F-doped CeO_2	Solution combustion method	NaF	10 mg L^{-1} methylene blue	UV	92.1% in 6 min	48
7	F-doped ZnO	Sol–gel method	NH_4F	10 mg L^{-1} DCF	Simulated solar radiation	88.4%	49
8	F-doped ZnO	Hydrothermal approach	NH_4FHF	10 mg L^{-1} DCF	UV	85% in 30 min	50
9	F-doped TiO_2	Modified sol–gel method	Trifluoroacetic acid	0.5 mg L^{-1} atrazine	UV and visible light	53.9 and 36.6% in 180 min	51
10	F-doped $(NH_4)_{0.33}WO_3$		HF	20 mg L^{-1} RhB	Near-infrared	83% in 180 min	52
11	F-doped reduced graphene oxide-Bi_2WO_6	One-step hydrothermal method	NaF	5 mg L^{-1} RhB	Visible-light	About 95% in 90 min	53
12	F-doped g-C_3N_4	—	NH_4F	10 mg L^{-1} PFOA	Visible-light	74.3% in 4 h	54
13	Cl-doped Bi_2MoO_6	Hydrothermal approach	NaCl	200 mL 10^{-5} M RhB	Visible-light	99.5% in 160 min	55
14	Br-doped $Bi_2O_2CO_3$	Hydrothermal approach	Cetyltrimethylammonium bromide	10^{-5} M RhB	UV-vis	100% in 30 min	56
15	I-doped $Bi_2O_2CO_3$	Hydrothermal approach	NaI	10^{-5} M RhB	Visible-light	100% in 6 min	57
16	N-doped TiO_2	Hydrothermal method	Urea	10 mg L^{-1} methylene blue	Visible-light	87.9% in 180 min	58
17	P-doped $CeVO_4$	Electrospinning process	$(NH_4)_2HPO_4$	20 mg L^{-1} levofloxacin	Simulated sunlight	92.9% in 140 min	59
18	S-doped covalent triazine	—	S	1 mg L^{-1} methyl orange	Visible-light	53.2% in 6 h	60

Shen *et al.* prepared original CTF-1 (original covalent triazine frameworks) and a series of CTFS*x* doped with different contents of S. The S-doped CTF exhibited excellent photocatalytic activity and cyclic stability compared to the original CTF-1. CTFS5 (covalent triazine frameworks doped with a mass of 0.02 g S) showed the best photocatalytic performance. The visible photocatalytic reaction showed a degradation rate of 53.2% for methyl orange and 84.7% for bisphenol A within 6 h. The degradation rate constants were 0.145 h^{-1} and 0.29 h^{-1}, which were 3.6 and 5.8 times higher than those of CTF-1, respectively. Further studies have shown that enhanced visible light absorption, reduced free carrier recombination, rapid separation and transfer of photogenerated electrons and holes, and increased –OH oxidation capacity are important factors in the significant enhancement of their photocatalytic activity.[60]

In order to better demonstrate the synthesis and photocatalytic applications of F-doped materials/other element-doped materials, their preparation methods and photocatalytic properties are summarised in Table 1.

2.2 Electrocatalysis

2.2.1 CO_2 reduction reaction. With the rapid development of industry, the excessive emissions of carbon dioxide have brought about climate problems and the greenhouse effect.[61–63] The conversion of CO_2 *via* carbon dioxide electrocatalytic reduction reactions (CO_2RR) into fuels and chemical feedstocks using renewable energy sources is a promising way to alleviate the growing demand for energy.[64]

Ni *et al.* synthesized fluorine-doped caged porous carbon (F-CPC) as an efficient catalyst for CO_2RR by using a polymer-derived method. Fig. 5a shows the synthesis process of the F-CPC sample. The optimized F-CPC has a large specific surface area, medium mesopores, and abundant micropores as well as a high electrical conductivity. When used as a catalyst for the CO_2RR, F-CPC exhibits faradaic efficiency (FE) of 88.3% for CO at −1.0 V *vs.* RHE with a current density of 37.5 mA cm^{-2}. Fluorine doping can adjust the electronic structure by generating a positive charge density, thus enhancing the adsorption of *COOH and inhibiting the hydrogen evolution reaction (HER).[30] Han *et al.* fabricated a fluorine-tuned single-atom catalyst with an ultrathin nanosheet morphology (only ~1.25 nm) and high Ni content of 5.92 wt% by a polymer-assisted pyrolysis approach (Fig. 5b). As a result, this catalyst with unique structural features exhibits a remarkable electrocatalytic performance for CO_2-to-CO conversion with FE over 95% in a wide potential range and an outstanding CO evolution rate of 1146 mmol g_{cat}^{-1} h^{-1} at −0.97 V *vs.* RHE. F-doping alters the electronic configuration of the central Ni–N_4 site, thereby lowering the energy barrier to CO_2 activation, which facilitates the generation of key *COOH intermediates.[31] Chen *et al.* reported the facile construction of F-doped Fe-N-C single-site catalysts (SSC) and the electron-withdrawing character of fluorine could stabilize Fe^{3+} sites, which promotes the CO faradaic efficiency (FE_{CO}) from the volcano-like highest value (88.2% @ −0.40 V) to the high plateau (>88.5% @ −0.40 to −0.60 V), with a much-increased partial current (J_{CO}) (from 3.24 to 11.23 mA cm^{-2}). The fluorine doping stabilizes the Fe^{3+} sites and enriches the defects, thus promoting the CO_2RR thermodynamically, inhibiting competitive hydrogen evolution reactions, and increasing the electroactive surface area kinetically, improving charge transfer. The Fe-FN-C was synthesized by a convenient adsorption–pyrolysis route, as shown in Fig. 5c.[29]

2.2.2 N_2 reduction reaction. NH_3 plays a key role in the Earth's ecosystem and is widely used as a reactive nitrogen

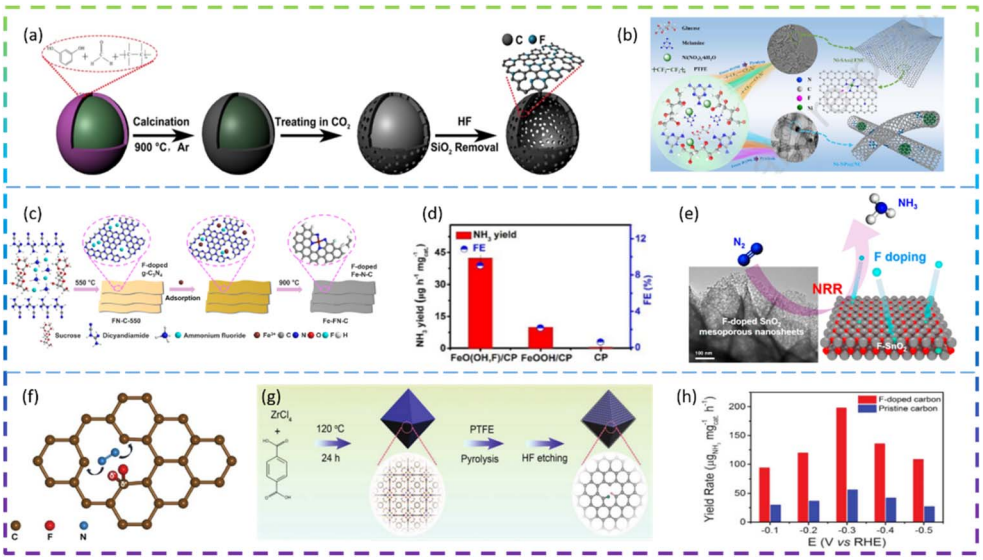

Fig. 5 (a) Schematic illustration to the formation process of the fluorine-doped cagelike porous carbon (F-CPC). (b) Schematic illustration for the formation and structures of Ni-SAs@FNC and Ni-NPs@NC. (c) Schematic diagram for the synthesis of Fe-FN-C. (d) NH_3 yields and FEs of different electrodes at −0.60 V after electrolysis for 2 h. (e) Schematic diagram of electrocatalytic reduction of N_2 on fluorine-doped SnO_2 porous nanosheets. (f) Schematic of the atomic structure of fluorine-doped carbon. (g) Schematic of the synthetic procedure for F-doped carbon. (h) Yield rate for NH_3 of F-doped carbon and pristine carbon at different applied potentials.

block in the manufacture of fertilizers, dyes, and pharmaceuticals, as well as a clean source of energy. The electrocatalytic conversion of nitrogen to ammonia *via* the N_2 reduction reaction (NRR) provides a clean and scalable method for synthesizing ammonia under ambient conditions.[65–69]

Zhu *et al.* reported that the NRR activity of β-FeOOH nanorods can be greatly improved by simple F-doping. When tested at −0.60 V *vs.* the reversible hydrogen electrode (RHE) in 0.5 M $LiClO_4$, these β-FeO(OH, F) nanorods obtain optimal NH_3 yield (42.38 μg h^{-1} mg_{cat}^{-1}) and FE (9.02%), much higher than those of pristine β-FeOOH (10.01 μg h^{-1} mg_{cat}^{-1}, 2.16%) (Fig. 5d). DFT calculations show that the reaction energy barrier for β-FeO(OH, F) (0.24 eV) is lower than that for β-FeOOH (0.59 eV), resulting in an enhanced activity. Overall, their theoretical calculations show that the performance of the NRR can be significantly improved by the substitution of OH groups by F atoms and therefore β-FeO(OH, F) is a promising electrocatalyst for the NRR, which agrees well with the experimental electrochemical results.[33] Liu *et al.* developed fluorine (F)-doped SnO_2 mesoporous nanosheets on carbon cloth (F-SnO_2/CC) as an efficient NRR electrocatalyst. In 0.1 M Na_2SO_4, F-SnO_2/CC exhibited an NH_3 yield of 19.3 μg h^{-1} mg^{-1} and an FE of 8.6% at −0.45 V. It has high durability and is superior to most of the reported NRR catalysts. Specifically, the DFT results reveal that F-doping increases conductivity and increases the density of positive charges on the active Sn sites, thereby reducing the reaction energy barrier and enhancing NRR activity. The schematic diagram of the electrocatalytic reduction of N_2 on fluorine-doped SnO_2 porous nanosheets is shown in Fig. 5e.[34] Yuan *et al.* reported that a non-metallic fluorine doped carbon improved the efficiency of the electrochemical NRR. The fluorine-doped carbon exhibits better NRR performance than the undoped carbon, with a peak ammonia production rate (6.9 μg h^{-1} cm^{-2}) and a corresponding high faradaic efficiency (12.1%) at −0.55 V *versus* the reversible hydrogen electrode (RHE). The doping of fluorine allows the electron distribution of the carbon to be adjusted, which provides positively charged carbon sites that are more likely to adsorb N_2 rather than H^+ under acidic water conditions. Doping of the carbon skeleton with F atoms can effectively lead to the positive polarisation of adjacent carbon atoms. These strongly polarised carbon atom positions can serve as effective locations for the adsorption of protons by the N_2 molecule (Fig. 5f).[35] Liu *et al.* introduced F atoms into a 3D porous carbon framework (F-doped carbon) for N_2 electroreduction and developed a highly efficient metal-free catalyst. Fig. 5g exhibits the synthetic procedure of F-doped carbon. At −0.2 V *versus* the reversible hydrogen electrode (RHE), the F-doped carbon achieves the highest FE of 54.8% for NH_3, which is 3.0 times as high as that (18.3%) of pristine carbon frameworks. It is worth noting that at −0.3 V *versus* RHE, the yield rate of F-doped carbon for NH_3 reaches 197.7 μg_{NH_3} mg_{cat}^{-1} h^{-1} (Fig. 5h). Mechanistic studies have shown that the improved electroreduction performance of F-doped N_2 is mainly due to the enhanced N_2 binding strength and easier dissociation of N_2 into $*N_2H$. Due to the difference in electronegativity between F and C atoms, F bonds with C atoms to form Lewis acid sites. As a result, the repulsion between the Lewis acid site and the proton H inhibits the activity of the H_2 evolution reaction, thus improving the selectivity of the electroreduction of N_2 to NH_3.[32]

2.2.3 O_2 reduction reaction

2.2.3.1 2-Electron pathway reactions. Hydrogen peroxide (H_2O_2) is an important environmentally friendly chemical that is widely used in the chemical industry, sanitation, and environmental remediation. The current industrial synthesis of hydrogen peroxide is carried out by the anthraquinone process, which has the disadvantages of fragmented production, high energy consumption, the generation of large amounts of organic by-products, and the need to transport the resulting H_2O_2 to the point of use.[70,71] Therefore, the electrochemical synthesis of H_2O_2 *via* the two-electron pathway of the oxygen reduction reaction (ORR) becomes an attractive alternative method.

Zhao *et al.* prepared F-doped porous carbon with excellent performance for electrochemical synthesis of H_2O_2 by carbonization of MIL-53 (Al). The F content has an influence on the production of H_2O_2, and the best catalytic activity for H_2O_2 electrosynthesis is achieved when the F content is 3.41 at%. The resultant F-doped porous carbon (FPC) catalysts exhibited good H_2O_2 selectivity of 97.5–83.0% and the H_2O_2 production rate could reach 112.6–792.6 mmol h^{-1} g^{-1} over the potential range of 0.2 V to −0.3 *vs.* RHE (pH 1). The addition of $CF_{2,3}$ facilitates the adsorption of O_2 and the desorption of OOH, resulting in a high selectivity for the two-electron reduction reaction of oxygen. The synthetic process for the fabrication of F-doped porous carbon is shown in Fig. 6a.[72] Wang *et al.* used F to modify carbon nanotubes (CNT) and H_2O_2 was produced with a gas diffusion electrode (GDE) based on the F-doped CNT catalyst as cathode. The results show that F-doping can improve the oxygen reduction activity and the selectivity of H_2O_2, which in turn improves the yield of H_2O_2. The F-CNT prepared with 0.6 M HF (CNT-F-0.6) showed significantly higher hydrogen peroxide production (47.6 mg L^{-1}) and current efficiency (89.5%) than carbon nanotubes (29.6 mg L^{-1}, 70.1%) at a bias voltage of −1.3 V (*vs.* SCE) and pH 7, and still maintained high catalytic activity for five consecutive reaction cycles. The improved performance of the F-modified CNT-GDE can be attributed to the CF_2 and CF_3 on the F-doped CNT catalyst (Fig. 6b).[73] Zeng *et al.* synthesized an F-doped carbon electrocatalyst in an F_2 atmosphere. The fluorine-doped carbon was synthesized in a sealed fluidized bed, and the device is shown in Fig. 6c. H_2O_2 was generated *via* a two-electron pathway using F-doped carbon as the cathode. 3 h of electrolysis resulted in a H_2O_2 concentration of 2837.5 mg L^{-1} and a selectivity of 95.7%. And 12 cycles (3 h each) of H_2O_2 concentration remained constant, indicating good stability of the catalyst. Fluorine has high electronegativity and induces polarisation of adjacent carbon, creating active centers and increasing the force between oxygen and carbon. The X-ray photoelectron spectra (XPS) and DFT data confirm that the CF_2 bond type facilitates the adsorption of O_2 and the desorption of OOH, thereby increasing the ability of the catalyst to produce H_2O_2.[74]

2.2.3.2 4-Electron pathway reactions. The ORR is a key reaction in rechargeable metal–air cells and fuel cells, and has been

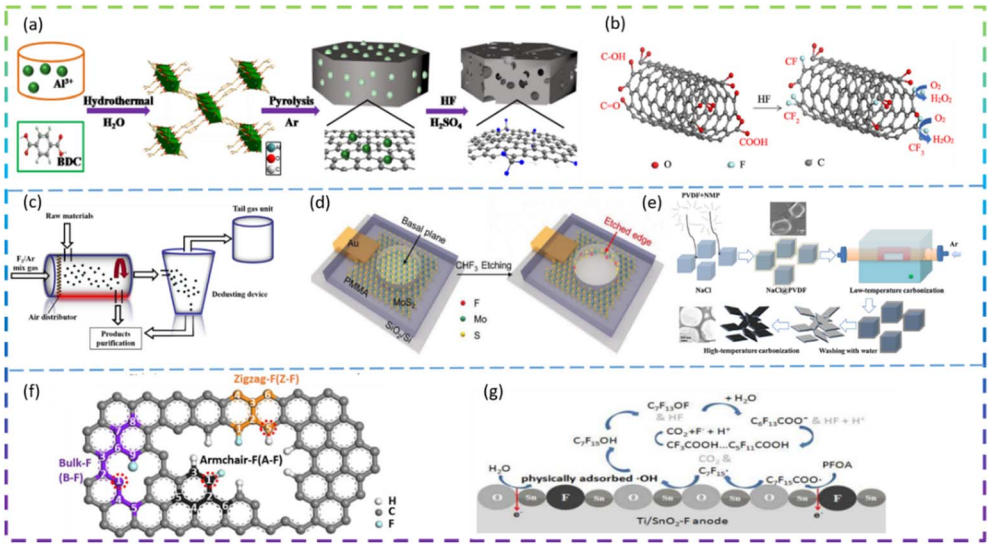

Fig. 6 (a) Procedure for the synthesis of F-doped hierarchically porous carbon catalysts. (b) Enhanced two-electron oxygen reduction process by F-CNT. (c) Schematic diagram of the synthesis device of F-doped carbon. (d) Schematic illustration of *in situ* creation and doping of etched edges on MoS_2 by CHF_3 plasma. (e) Illustration of the synthesis procedure for FC. (f) Schematic depicting the structures of A-F, B-F and Z-F. (g) Schematic diagram of PFOA degradation on the Ti/SnO_2-F electrode.

extensively studied due to the pollution problems caused by the use of fossil fuels.[75,76] Chang *et al.* firstly produced 2D porous F-doped carbon nanosheets by using polyvinylidene fluoride as precursor and NaCl as the template (Fig. 6e). FC-900 (pyrolyzed at 900 °C) shows an impressive ORR due to the large specific surface area (1031 $m^2\ g^{-1}$) and the highly active sites. The FC nanosheets exhibit high ORR activity as Pt/C catalysts under alkaline conditions due to the synergistic effect of defects and appropriate F dopants producing highly active sites, thus ensuring high-performance zinc–air batteries. When the samples were further calcined at 900 °C for different times, the ORR activity of the samples obtained improved slightly, indicating that the defects have much less influence on the ORR performance than the fluorine doping. The ORR activity on F-doped graphene was studied by DFT. In total, three kinds of F doping patterns are modeled for DFT calculation, namely, the F doped on bulk (denoted as B-F), armchair edge (denoted as A-F), and zigzag edge (denoted as Z-F), with their structures shown in Fig. 6f.[38]

2.2.4 H_2 evolution reaction. Energy and the environment are the most important issues involved in the sustainable development of human societies. Hydrogen (H_2) is currently being explored as one of the potential next-generation energy carriers due to its unique characteristics such as its renewable nature, abundance, high gravimetric energy density, diverse production sources, and zero pollution.[77,78] Among the many methods of hydrogen production, hydrogen evolution by electrochemical reaction is a frontier area of research.

Zhang *et al.* used the CHF_3 plasma etching to create F-doped MoS_2 edge sites with enhanced HER performance and stability. The doping of the more electronegative fluorine atoms at the MoS_2 edge positions resulted in a fivefold enhancement in activity compared to the original edge and was attributed to a more moderate binding energy of the hydrogen species (Fig. 6d). The study provides two-dimensional materials as a platform for understanding edge site doping effects at the atomic level and offers a new avenue for the design of efficient catalysts.[37]

2.2.5 Degradation of PFOA. The hazards of PFOA have been described previously and in the last decade electrochemical oxidation has become an effective method for degrading PFOA in water, which can be operated in a common electric field and without the necessity of any chemical additives.

Yang *et al.* prepared an F-doped Ti/SnO_2 (Ti/SnO_2-F) electrode using tin tetrafluoride as a novel single-source precursor, which provided a promising anode material for wastewater treatment containing highly stable PFOA. The Ti/SnO_2-F electrode has higher oxidation activity and longer service life than the Ti/SnO_2–X (X = Cl, Br, I, Sb) electrode, decomposing over 99% of the PFOA (50 mL 100 mg L^{-1}) in 30 min of electrolysis. The similar ionic radii of F and O as well as the strong electronegativity of F lead to high electrochemical stability and a smooth surface, generating weakly adsorbed ·OH. Details of the mechanism of PFOA degradation on the Ti/SnO_2-F electrode are shown in Fig. 6g.[36]

2.2.6 Doping with other halogen elements. Experimental studies on the application of doping with other halogen elements in the field of electrocatalysis are scarce, but some researchers have carried out relevant theoretical calculations. For example, Zou *et al.* prepared Cl-doped ultrathin graphdiyne (denoted as Cl-GDY) by a corrosion strategy. The Cl-GDY can afford a relatively high NH_3 yield rate of 10.7 μg h^{-1} cm^{-2} associated with a faradaic efficiency of 8.7% at −0.45 V and −0.4 V *versus* the reversible hydrogen electrode, respectively. DFT calculations show that Cl doping reduces the limiting potential by 0.11 eV, indicating that Cl doping favors N_2

Table 2 Synthesis and electrocatalytic properties of F-doped materials/other element-doped materials

No.	Materials	Preparation	Fluorine source/other doping element sources	Application	Performance	Ref.
1	F-doped cage like porous carbon	Polymer-derived method	HF	CO_2 reduction reaction	FE of 88.3% for CO at −1.0 V *vs.* RHE with a current density of 37.5 mA cm^{-2}	30
2	F-doped single Ni atoms supported on graphitized carbon	Polymer-assisted pyrolysis approach	PTFE	CO_2 reduction reaction	FE over 95% in a wide potential range and an outstanding CO evolution rate of 1146 mmol g_{cat}^{-1} h^{-1} at −0.97 V *vs.* RHE	31
3	F-doped Fe-N-C	Convenient adsorption–pyrolysis route	NH_4F	CO_2 reduction reaction	FE_{CO} (>88.5% @ −0.40 to −0.60 V), J_{CO} (11.23 mA cm^{-2})	29
4	F-doped β-FeOOH		NaF	N_2 reduction reaction	NH_3 yield (42.38 μg h^{-1} mg_{cat}^{-1}) and FE (9.02%)	33
5	F-doped SnO_2/CC	Facile solvothermal approach	NaF	N_2 reduction reaction	NH_3 yield of 19.3 μg h^{-1} mg^{-1} and a faradaic efficiency of 8.6% at −0.45 V (*vs.* RHE)	34
6	F-doped carbon	—	PTFE	N_2 reduction reaction	Peak ammonia production rate (6.9 μg h^{-1} cm^{-2}) and a corresponding high faradaic efficiency (12.1%) at −0.55 V *vs.* RHE	35
7	F-doped porous carbon	Polymer-assisted pyrolysis approach	PTFE	N_2 reduction reaction	FE of 54.8% for the NH_3 product at −0.2 V *vs.* RHE, the yield rate for NH_3 reached 197.7 μg_{NH_3} mg_{cat}^{-1} h^{-1}	32
8	F-doped hierarchically porous carbon	—	HF	Oxygen reduction reaction	H_2O_2 selectivity of 97.5–83.0% and the H_2O_2 production rate reached 112.6–792.6 mmol h^{-1} g^{-1} in the potential range of 0.2 V to −0.3 V *vs.* RHE (pH 1)	72
9	F-doped modified carbon nanotubes	—	HF	Oxygen reduction reaction	H_2O_2 production (47.6 mg L^{-1}) and current efficiency (89.5%) at a bias voltage of −1.3 V (*vs.* SCE) and pH 7	67
10	F-doped carbon	—	F_2	Oxygen reduction reaction	The H_2O_2 concentration and selectivity of the catalyst can reach 2837.5 mg L^{-1} and 95.7% after electrolysis for three hours	73
11	F-doped MoS_2 edge electrodes	Plasma etching strategy	CHF_3	Hydrogen evolution reactions	Overpotential of 160 mV ($j = -0.02$ nA μm^{-1}), Tafel slope of the etched edge: 136 mV dec^{-1}	37
12	F-doped Ti/SnO_2	—	SnF_4	Degradation of PFOA	Decomposed over 99% of PFOA (50 mL, 100 mg L^{-1}) within 30 min of electrolysis	36
13	Cl-doped ultrathin graphdiyne	Corrosion strategy	Cl_2	N_2 reduction reaction	NH_3 production rate of 10.7 μg h^{-1} cm^{-2} and a high FE of 8.7% at −0.45 V and −0.4 V, respectively	79
14	S,N dual-doped graphene-like carbon	Polymer-assisted pyrolysis	Dibenzyl sulfide and melamine	Oxygen reduction reaction	—	81
15	P-doped Ag	—	NaH_2PO_2	Hydrogen evolution reactions	Overpotential of 78 mV to drive 10 mA cm^{-2} in 0.5 M H_2SO_4	82
16	S-doped graphene	Solution-phase method	—	N_2 reduction reaction	Ammonia production rate of 27.5 μg_{NH_3} mg_{Au}^{-1} h^{-1} with a FE of 2.3% at −0.5 V	83

reduction.[79] Luo *et al.* studied the possibility of using transition metal (TM)/MXene as a catalyst for the NRR using DFT, in which TM is an Fe atom, and MXene is pure $Ti_3C_2O_2$ or $Ti_3C_2O_{2-x}$ doped with N/F/P/S/Cl. Non-metallic doping has an impact on catalytic performance compared to pure $Ti_3C_2O_2$, and among the catalysts tested, materials doped with F and S were considered to be better NRR candidates.[80]

2.2.7 Doping with non-metallic elements. Recent studies have shown that doping, edges and defects can effectively optimize the charge/spin distribution and thus alter the chemisorption and subsequent electron transfer of intermediates. Li *et al.* synthesized S,N dual-doped graphene-like carbon nanosheets *via* a simple pyrolysis of a mixture of melamine and dibenzyl sulfide as efficient metal-free electrocatalysts for the ORR. Compared to single doping, S,N double-doped graphene-like carbon nanosheets exhibit enhanced activity towards the ORR and excellent durability in both basic and acidic media compared to conventional Pt/C electrocatalysts. The results show that the doping effect of the ORR in S,N double-doped carbon materials relies heavily on the synergistic effect of the S and N atoms.[81]

Ji *et al.* developed P-doped Ag nanoparticles embedded in N-doped carbon nanoflakes (denoted as P-Ag@NC) for effective hydrogen evolution electrocatalysis. P-Ag@NC exhibits stronger catalytic activity than undoped Ag@NC, requiring an overpotential of 78 mV to drive 10 mA cm^{-2} in 0.5 M H_2SO_4, which is 198 mV lower than for Ag@NC. In addition, the catalyst exhibits strong long-term electrochemical durability. DFT calculations show that P doping optimizes the hydrogen adsorption free energy to a more thermoneutral value.[82]

Li *et al.* demonstrated sulfur-doped graphene (S-G) can be utilized to stabilize ultrafine (sub-2 nm) $Au_{25}(PET)_{18}$ clusters to enable stable NRR without significant structural degradation. The Au_{25}@S-G exhibits an ammonia yield rate of 27.5 μg_{NH_3} $mg_{Au}^{-1} \cdot h^{-1}$ at −0.5 V with faradaic efficiency of 2.3%. Sulfur dopants play a key role in stabilizing the chemical state and coordination environment of the Au atomic clusters.[83]

In order to better demonstrate the synthesis and electrocatalytic applications of F-doped materials/other element-doped materials, their preparation methods and electrocatalytic properties are summarised in Table 2.

3 Applications and synthetic strategies for F-doped materials in rechargeable ion batteries

3.1 Lithium-ion batteries

3.1.1 Anode materials for LIBs. In recent years, LIBs have enjoyed great success as energy storage systems and are widely used in transportation and electronics.[84–86] Carbonaceous materials have been extensively investigated in commercial anode materials due to their environmental friendliness, low cost, good electronic conductivity, and long cycle life.[87,88] However, they still struggle to meet the growing market demand due to their limited theoretical capacity (372 mA h g^{-1}) and potential safety concerns.[89] Therefore, the development of stable, high-capacity anode materials is key to the realization of high-energy lithium batteries.

Fluorine doping is used extensively in electrodes to optimize their electrochemical properties. For example, Bai *et al.* synthesized an F-doped $Li_4Ti_5O_{12}$ anode material *via* the solid-state reaction. The F doping had no effect on the crystal structure of $Li_4Ti_5O_{12}$ and the particle size of the samples remained at a uniform size of about 1 μm. A comparison of Fig. 7a left and

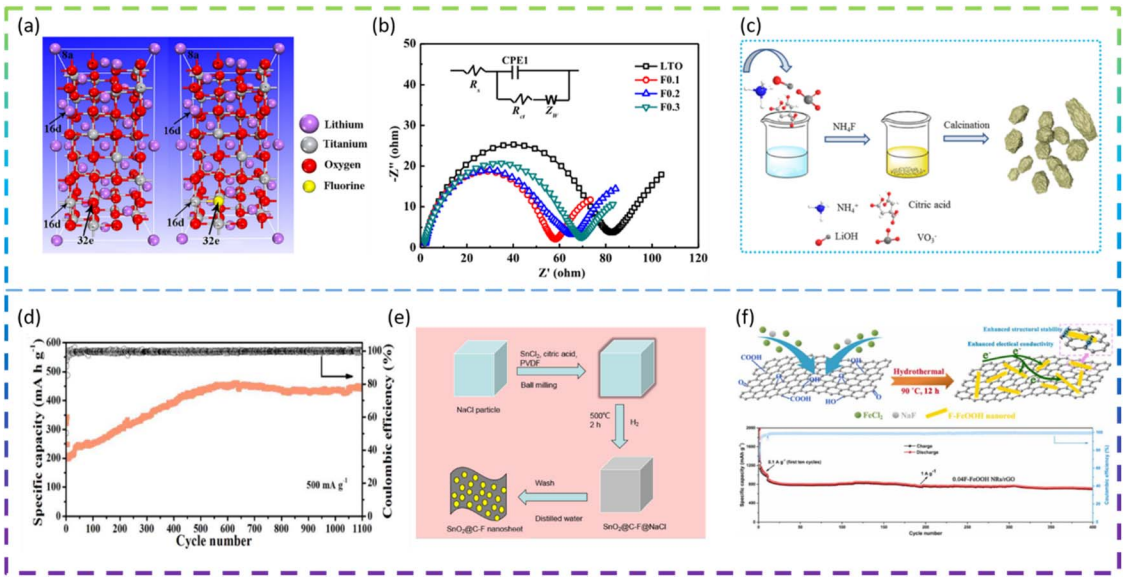

Fig. 7 (a) The crystal structures of $Li_{21}Ti_{27}O_{64}$ and $Li_{21}Ti_{27}O_{63}F_1$. (b) EIS curves (Nyquist plots) of all samples. (c) Preparation scheme for F-doped Li_3VO_4. (d) Long-term cycling (at 500 mA g^{-1} for 1100 cycles except for the first five cycles at 100 mA g^{-1}) for 5 at% F-doping. (e) Schematic of the synthetized porous SnO_2@C-F mesoporous nanosheets. (f) Diagram of the F-FeOOH NRs/rGO synthesis process and long-term cycling performance of 0.04F-FeOOH NRs/rGO at 1 A g^{-1}.

right images indicates that the molecular structure of $Li_4Ti_5O_{12}$ has not changed after F doping and also that it belongs to the *Fd3m* space group, except that the unit-cell contains one F atom at 32e sites replacing one O atom (Fig. 7a). In addition, the best performing material $Li_4Ti_5O_{11.9}F_{0.1}$ delivers superior rate capacities of 165, 162.1, 160.0, 142.3, 125.1, and 99.2 mA h g^{-1}, at 0.2C, 0.5C, 1C, 3C, 5C, and 10C, respectively, which are higher than those of $Li_4Ti_5O_{12}$ (150.0, 135.0, 123.5, 93.7, 76.4, and 56.8 mA h g^{-1} at the same C rates), and the cycling retention is 82.7% after 150 cycles at 5C. The $Li_4Ti_5O_{11.9}F_{0.1}$ electrode has higher charge transfer kinetics (Fig. 7b), lower electrode polarisation, and a higher lithium-ion diffusion coefficient than other electrodes.[90]

Liu *et al.* synthesized a series of F-doped Li_3VO_4 samples as anode materials for LIBs by a modified sol–gel method for the first time (Fig. 7c). The results show that the 5 at% F-doped sample has a long cycle life (1100 cycles at 500 mA g^{-1}, except for the first five 100 mA g^{-1} cycles) (Fig. 7d) and an optimized rate performance (255 mA h g^{-1} at 1000 mA g^{-1}), which is better than for the undoped sample. The doping of F leads to the appearance of oxygen vacancies and a reduction of the band gap, which effectively improves the electronic conductivity, the reduction of the electron and ion transport energy barriers, the complete rearrangement of the structure, the optimization of the SEI layer and the appearance of nanosheets.[91]

Feng *et al.* developed novel fluorine-doped porous SnO_2@C (SnO_2@C-F) nanosheets as an anode material for LIBs by a facile ball milling method with the NaCl template (Fig. 7e). The porous SnO_2@C-F nanosheet samples exhibited excellent electrochemical capacity (821 mA h g^{-1} at 200 mA g^{-1} after 100 cycles), excellent rate capacity (816.62, 684.46, 579.2, 476.08, 410.94, 361.64, 324.1 and 734.0 mA h g^{-1}, respectively) and long-term cycling stability (419.4 mA h g^{-1} at 2.0 A g^{-1} after 800 cycles). The formation of metal fluorides (Sn–F bond) and the strong electronic coupling between fluorine-doped carbon and SnO_2 nanoparticles can greatly improve the structural stability and electronic conductivity of SnO_2 negative electrode materials.[92]

Jin *et al.* synthesized F-doped $Ni_3V_2O_8$ nanorods as an anode material for LIBs *via* a molten-salt method. The F-doped $Ni_3V_2O_8$ nanorods have an initial coulombic efficiency of 90.8%, better cycling performance (983 mA h g^{-1} after 100 cycles at 200 mA g^{-1}), and excellent long-term stability (616 mA h g^{-1} after 500 cycles at 2000 mA g^{-1}). The results show that the one-dimensional F-doped oxygen-vacancy containing $Ni_3V_2O_8$ nanorods accelerate the migration of Li^+ ions and improve the electrochemical reaction kinetics.[93]

Zhu *et al.* synthesized novel hybrids of fluorine-doped FeOOH nanorods/reduced graphene oxide (F-FeOOH NRs/rGO) as anode materials for LIBs *via* a simple one-step hydrothermal method (Fig. 7f). Various amounts of NaF (1, 2 and 5 mM) were used to fabricate the hybrids with different F contents, which were denoted as 0.02F-FeOOH NRs/rGO, 0.04F-FeOOH NRs/rGO and 0.1FFeOOH NRs/rGO, respectively. As a result, the 0.04F-FeOOH NRs/rGO hybrid shows excellent lithium storage performance of 1207.4 mA h g^{-1} after 160 cycles at 0.1 A g^{-1}. In addition, it exhibits impressive rate capability and long-term recyclability (701.4 mA h g^{-1} at 1 A g^{-1} after 400 cycles) (Fig. 7f). The doping of F not only improves the electrical conductivity of FeOOH but also contributes to the formation of a large number of fine nanoparticles that shorten the transport distance of Li^+ and provide more electroactive sites for the storage of Li^+.[94]

Zhao *et al.* fabricated fluorine-doped $ZnFe_2O_4$ (ZFO-F) as an anode material for LIBs *via* a quick quenching method. The results show that the sample with the optimum amount of F doping has the smallest charge transfer resistance, the highest specific capacity of 950 mA h g^{-1} after stabilization at 0.5 A g^{-1}, and excellent rate performance, up to 312 mA h g^{-1} at a high current density of 5 A g^{-1} while it is only 200 mA h g^{-1} for pure $ZnFe_2O_4$. It was shown that the successful doping of the element F into ZFO brought about an abundance of active centers and improved electronic conductivity.[95]

3.1.2 Cathode materials for LIBs. With the increasing demand for high-power and high-energy-density batteries, large-scale research into cathode materials for LIBs has emerged. Song *et al.* synthesized $Li[Li_{1/6}Ni_{1/6}Co_{1/6}Mn_{1/2}]O_{2-x}F_x$ ($x = 0.00$ to 0.07) materials as cathode materials for LIBs with low temperature heat treatment (700 °C). With the addition of fluorine, the irreversibility of the first cycle is suppressed and the reversible capacity increases significantly (Fig. 8a). The reduction in irreversibility is mainly due to the addition of fluorine increasing the first cycle efficiency of the Li_2MnO_3-like fraction. The presence of fluorine promotes the reduction of cobalt and manganese ions in the lithium-rich layered oxide, while the reduced transition metal (TM) ions inhibit the structural changes.[96] Gao *et al.* synthesized F-doped $LiFePO_4$/C materials using a co-precipitation method followed by high-temperature treatment with a hydrofluoric acid source. Analysis of the structure shows that doping with F can change the lattice parameters, increase the lattice volume, change the interatomic distances, narrow the band gap and rearrange the electron cloud. This is due to the different ionic radii and electronic configurations of F^- and O^{2-}. Analysis of morphology and particle size shows that F-doping promotes the growth of primary particles. Electrochemical analysis shows that the F-doped $LiFePO_4$/C samples have better high-rate performance and cycling life than the undoped $LiFePO_4$/C composites (Fig. 8b). Doping with F improves the inherent disadvantages of the $LiFePO_4$ material, increases the electronic conductivity, accelerates the diffusion coefficient of Li^+ ions and improves the stability of the structure.[97]

Wang *et al.* employed F doping in improving the electrochemical performance of the Li_2MnSiO_4 cathode material. The results show that $Li_2MnSiO_{3.97}F_{0.03}$/C with the best electrochemical performance provides an initial specific discharge capacity of 279 mA h g^{-1} at a current density of 25 mA g^{-1} from 1.5 V to 4.8 V. In addition, it maintains a higher capacity (201 mA h g^{-1}) after 50 cycles than Li_2MnSiO_4 without F (145 mA h g^{-1}). Firstly, F doping not only broadens the lattice parameters but also reduces the particle size, which synergistically improves the Li^+-ion diffusion of Li_2MnSiO_4. Secondly, F doping improves the electronic conductivity of Li_2MnSiO_4/C by inhibiting the formation of C–O bonds in the carbon layer. At

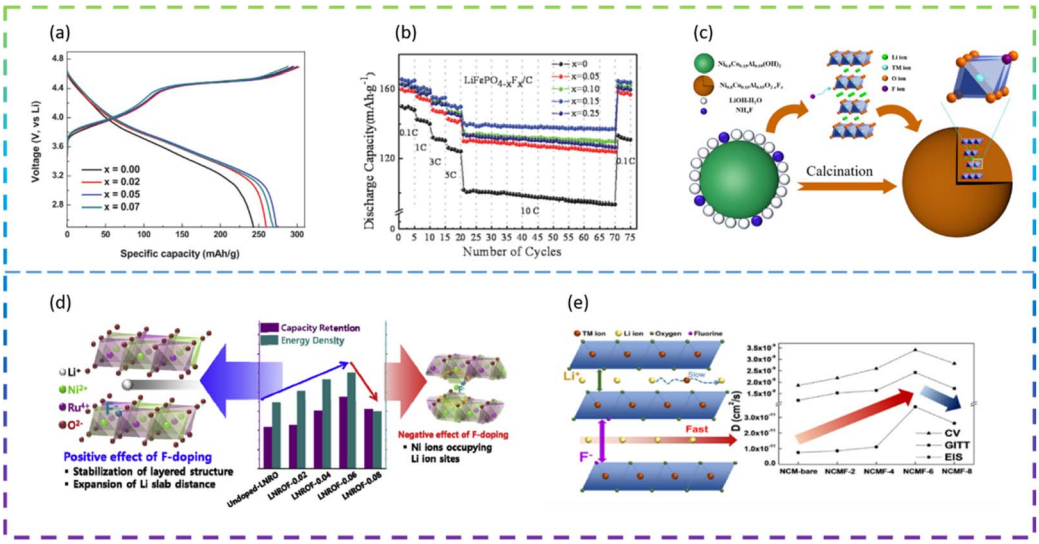

Fig. 8 (a) Initial charge/discharge curves. (b) Rate and cycle performances of undoped and F-doped $LiFePO_4$/C samples. (c) Schematic illustration of the *in situ* synthesis route for the F-doped $LiNi_{0.8}Co_{0.15}Al_{0.05}O_{2-x}F_x$ ($0 \leq x \leq 0.1$) composite powders. (d) Positive and negative effects of F-doped $Li_{1.15}N_{i0.275}Ru_{0.575}O_2$. (e) Comparison of Li-ion diffusion coefficients of the samples measured by CV, GITT, and EIS analysis.

the same time, F doping improves the crystallinity of Li_2MnSiO_4 and stabilizes the crystal structure.[98]

Choi *et al.* synthesized F-doped $Li_{1.15}Ni_{0.275}Ru_{0.575}O_2$ cathode structures (LNROF-x, $0 < x < 0.1$) using a facile solid-state reaction. The long life cycle and rate performance of the F-doped $Li_{1.15}Ni_{0.275}Ru_{0.575}O_2$ material can be attributed to the stronger structural stability of the metal–F bond than the metal–O bond and the increased diffusive movement of the lithium ions due to the increased Li sheet spacing. Nevertheless, excessive F doping causes the performance of LNROF-0.08 to deteriorate, with increased resistance to Li^+-ion movement and Li/Ni anti-location defects leading to a lower diffusion coefficient (Fig. 8d).[99]

Wang *et al.* synthesized F^- doped $LiNi_{0.8}Co_{0.15}Al_{0.05}O_2$ ($LiNi_{0.8}Co_{0.15}Al_{0.05}O_{2-x}F_x$ ($0 \leq x \leq 0.1$)) as LIB cathode materials by an *in situ* modified method (Fig. 8c). The reversible discharge specific capacity of the half-cell assembled with $LiNi_{0.8}Co_{0.15}Al_{0.05}O_{1.96}F_{0.04}$ composite electrodes was 157.8 mA h g^{-1}, with a capacity retention of 98.3% after 100 cycles at 2.0C and 25 °C. Even at a high temperature of 60 °C and a high current density of 5.0C, it was still possible to reach a discharge specific capacity of 142.6 mA h g^{-1} with a capacity retention of 89.1%. The significant improvement in lithium storage performance is mainly attributed to the introduction of F^- ions into the lattice, replacing the metal–O bond with a stronger metal–F bond, which not only effectively stabilizes the main structure and maintains structural integrity, but also prevents the erosion of HF and inhibits the increase in polarisation during continuous cycling.[100]

Kim *et al.* prepared Ni-rich ternary cathode materials (NCM) doped with various amounts of F dopant by a solid-state reaction method. The F-doped cathode material exhibited better cycling and rate performance compared to the undoped NCM samples, due to the relatively strong bond between the transition metal and F and the improved Li^+ ion transport behavior. However, when the F doping exceeds the optimum value, the performance of LIBs deteriorates due to the deterioration of Li^+ ion transport caused by Li/Ni anti-substitution defects (Fig. 8e).[101]

3.1.3 Other element-doped LIBs. Doping strategies have proven to be an effective way to enhance the electrochemical properties of materials, and there are numerous reports on the doping of various metal cations (*e.g.*, V^{5+}, Mn^{3+}, Fe^{3+}) in the Li (or Ti) site. In addition, doping of non-metal ions (*e.g.*, Cl^-, Br^-, I^-) on the O site is also attracting attention. Liu *et al.* synthesized a Cl-doped $LiFePO_4$/C (LFP/C) cathode material for LIBs by a high-temperature solid phase method. The initial capacity of the Cl-doped LFP/C electrode reached 164.1 mA h g^{-1} at 0.1C, approximately 96.53% of the theoretical capacity (170 mA h g^{-1}). The Cl-doped LFP/C electrode material achieves a reversible capacity of 105.3 mA h g^{-1} at 10C with a reversible capacity retention of 91.5% after 500 cycles, which is much higher than that of the undoped LFP/C electrode material (62.7%). Cl doping can effectively change the microstructure of LFP and improve the electronic conductivity and lithium ion diffusion rate, thus significantly improving the electrochemical performance of LFP/C electrode materials.[102]

Kim *et al.* synthesized Br-doped $Li_4Ti_5O_{12-x}Br_x$ ($x = 0$, 0.1, 0.3, 0.5, and 0.7) (LTOBrx) anode materials for LIBs by a conventional solid-state reaction technique. The LTOBr0.5 sample had a maximum capacity of 125 mA h g^{-1} at 1C compared to 115 mA h g^{-1} for pure LTO. However, the highly Br-doped sample (LTOBr0.7) showed a slight decrease in capacity. Most of the Br ions are located on the surface/interface of the agglomerated particles, rather than in the bulk lattice. As a result, electrons and lithium ions form narrow conduction paths on their surfaces/interfaces. The presence of these narrow surface conductive tubes improves the rate capability of the LTOBr sample during the charge/discharge process.[103]

Wang *et al.* synthesized Br-doped $Li_4Ti_5O_{12}$ microspheres (LTOS) as anode materials for LIBs using a cetyltrimethylammonium hydroxide-assisted hydrothermal method and further calcination. Among the doped samples, 0.2Br-LTOS has excellent rate performance and cycling capability. Even at 50C and 60C, its specific capacities are still as high as 101 and 96 mA h g^{-1}, respectively. Moreover, its capacity retention ratio is about 87.8% after 1000 cycles at 10C, which is higher than the 76.5% of pure LTOS. The spherical morphology and spinel-type microstructure of LTOS remain unchanged after proper Br doping, but the relative content of Ti^{3+} increases, which facilitates the rapid transport of electrons and ions.[104]

3.2 Sodium-ion batteries

3.2.1 Anode materials for SIBs. LIBs are the most favourable energy storage device but are limited by their high cost, shortage of naturally stored lithium, uneven distribution of lithium resources, and rough recycling, which are obstacles to further scaling up the production of LIBs.[105–107] The charge and discharge characteristics and mechanisms are similar between SIBs and LIBs. SIBs have recently attracted interest due to their low cost, environmental friendliness, abundance of sodium, and wide distribution, and SIBs are considered a promising alternative to energy storage devices.[108,109] In general, both LIBs and SIBs rely on the reversible intercalation and deintercalation processes of lithium or sodium ions between the positive and negative electrodes of the electrolyte during charging and discharging to complete the energy conversion. As an integral part of SIBs, negative electrode materials such as carbon-based materials, oxides, alloys and sodium superionic conductor (NASICON) compounds have been extensively investigated.[110–114] It is important to develop suitable anode materials with high capacity, long cycle life, and excellent rate performance.

Chen *et al.* synthesized F-doped $Na_2Ti_3O_7$ nanorods by a solid-phase method as an anode for SIBs. In Fig. 9a and b, the cell with $NTOF_{0.3}$ electrodes showed the best electrochemical performance. The specific capacity of the F-doped $Na_2Ti_3O_7$ sample is 30% higher than that of pure $Na_2Ti_3O_7$, due to the increased Na^+ diffusion coefficient. The F doping improves the charge transfer resistance of the material and the resulting material also exhibits better rate properties and cycling for more than 800 cycles.[115]

Wei *et al.* synthesized F-doped $Na_{1-2x}Ti_2(PO_4)_{3-x}F_x$ (denoted as NTP-F_x/C, $x = 0$, 0.02, 0.05, 0.10) as anode materials for SIBs by a sol–gel method. Among the F-doped composites, NTP-$F_{0.05}$/C shows the best electrochemical performance: the specific capacity decreases from 121 mA h g^{-1} to 85.8 mA h g^{-1} as the current density increases from 0.2C to 20C. It offers a specific discharge capacity of 62.5 mA h g^{-1} even at 30C, demonstrating superior rate capability (Fig. 9c). NTP-$F_{0.05}$/C also exhibits a high reversible capacity of 102.5 mA h g^{-1} at 10C and a retention capacity of 90% after 1000 cycles, demonstrating excellent cycling performance and structural stability. The results of the electrical analysis show that fluorine doping significantly enhances the diffusion kinetics of Na^+. Meanwhile, density functional theory calculations indicate that the F-doped nanotubes have excellent electrochemical properties due to their enhanced intrinsic ion/electron conductivity.[116]

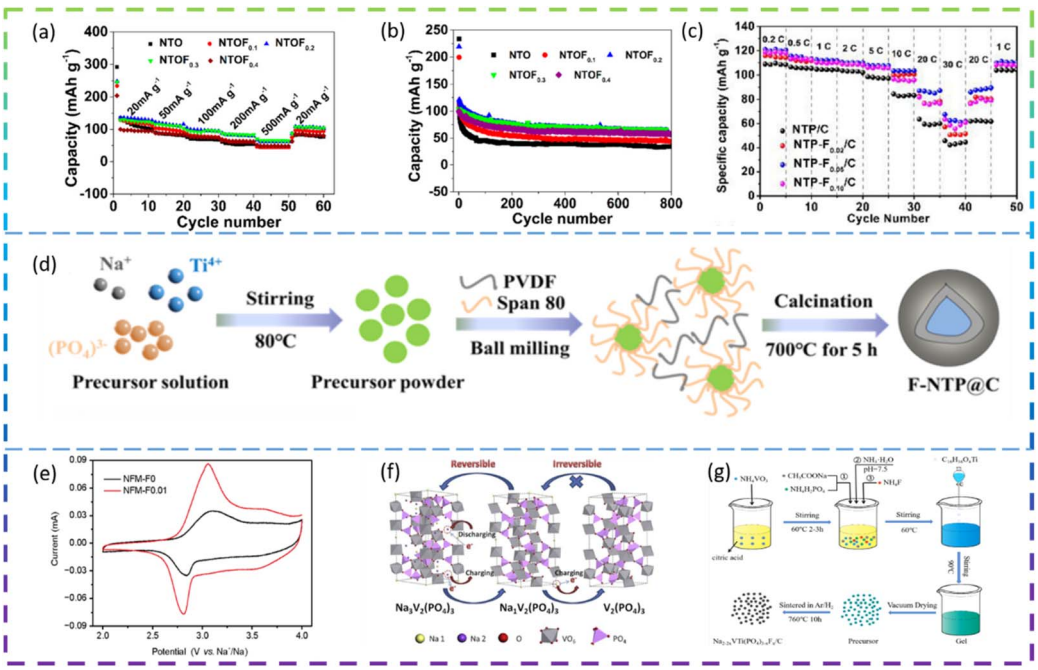

Fig. 9 (a) The specific capacity performance of NTO and NTOF*x* at different current densities. (b) The cycling properties of NTO and NTOF*x* at a current density of 100 mA g^{-1}. (c) Rate performance of $Na_{1-2x}Ti_2(PO_4)_{3-x}F_x$/C from 0.2C to 30C. (d) Schematic illustration of the synthetic route of F-NTP@C. (e) The first CV curves of NFM-F0 and NFM-F0.01 at a scan rate of 0.1 mV s^{-1}. (f) Schematic of the structural degradation of $Na_3V_2(PO_4)_3$. (g) Schematic illustration of the preparation process of $Na_{2-2x}VTi(PO_4)_{3-x}F_x$/C.

Deng *et al.* prepared fluorine-doped $NaTi_2(PO_4)_3$@C composite (F-NTP@C) anode materials for SIBs by a sol–gel method followed by a high temperature solid state method (Fig. 9d). The modified F-NTP@C material with a 3D porous structure exhibits excellent rate performance (108.7 mA h g^{-1} at 50C) and long cycle life (75.5% capacity retention after 2000 cycles at 10C). It also shows temperature adaptability over a wide range from 0 to 50 °C. By combining experimental data with theoretical calculations, it can be concluded that the enhanced electronic conductivity and fast Na^+ kinetics are attributed to the doping of F^- ions and the design of the 3D porous structure.[117]

3.2.2 Other element-doped SIB anodes. In addition, heteroatom doping (*e.g.* with S, P, N) is an effective means of modulating the chemical and physical properties of carbonaceous materials by creating defects and pores to modulate the electronic properties and increase the interlayer distance of carbon. Quan *et al.* synthesized sulfur-doped graphene (S-SG) *via* a one-pot method as an anode electrode material for SIBs. S-SG exhibited a high reversible capacity of 380 mA h g^{-1} after 300 cycles at 100 mA g^{-1}, an excellent rate performance of 217 mA h g^{-1} at a particularly high current density of 3200 mA g^{-1}, and a superior cycling performance of 263 mA h g^{-1} at 2.0 A g^{-1} over 1000 cycles. The results show that the prepared S-SG structure is highly disordered with large interlayer distances and a high number of active sites.[118]

Zhao *et al.* prepared N/P co-doped soft carbon nanoboxes (NPSC) as anodes for SIBs using petroleum pitch as raw material. At a high current density of 1 A g^{-1}, the NPSC can provide a high reversible capacity of 162 mA h g^{-1} for 3000 cycles. DFT calculations show that the N and P co-doped carbon has more electrons near the Fermi level, thus facilitating electron transport.[119]

3.2.3 Cathode materials for SIBs. The cathode material has always determined the performance of the battery and accounts for a large part of the overall battery cost. Therefore, research on cathode materials for SIBs can facilitate the process of application of SIBs. Zhang *et al.* synthesized F-doped O3-type $NaNi_{1/}$

Table 3 Synthesis and properties of F-doped material electrodes/other element-doped materials

No.	Materials	Preparation	Fluorine source/other doping element sources	Application	Specific capacity (mA h g^{-1})	Cycling number	Current rate (mA g^{-1})	Ref.
1	F-doped $Li_4Ti_5O_{12}$	Solid-state reaction	NH_4F	LIB anode	106.4	150	—	90
2	F-doped Li_3VO_4	Sol–gel method	NH_4F	LIB anode	450	1100	500	91
3	F-doped porous SnO_2@C	Ball milling method	PVDF	LIB anode	419.4	800	2000	92
4	F-doped $Ni_3V_2O_8$	Molten-salt method	NaF	LIB anode	616	500	2000	93
5	F-doped FeOOH	One-step hydrothermal method	NaF	LIB anode	701.4	400	1000	94
6	F-doped $ZnFe_2O_4$	Quick quenching method	NH_4F	LIB anode	850	500	500	95
7	$Li[Li_{1/6}Ni_{1/6}Co_{1/6}Mn_{1/2}]O_{2-x}F_x$	Solid state reaction method	LiF	LIB cathode	~650	300	—	96
8	F-doped $LiFePO_4$/C	Co-precipitation method	HF	LIB cathode	129.8	50	3400	97
9	F-doped Li_2MnSiO_4/C	Solid-state reaction	LiF	LIB cathode	201	50	25	98
10	F-doped $Li_{1.15}Ni0_{.275}Ru_{0.575}O_2$	Solid-state reaction	NH_4F	LIB cathode	150	100	20	99
11	F-doped $LiNi_{0.8}Co_{0.15}Al_{0.05}O_2$	Co-precipitation process	NH_4F	LIB cathode	149.9	100	—	100
12	F-doped $Na_2Ti_3O_7$	Solid-phase method	NaF	SIB anode	~85	800	100	115
13	F-doped $NaTi_2(PO_4)_3$/C	Sol–gel method	NaF	SIB anode	67.3	1000	1330	116
14	F-doped $NaTi_2(PO_4)_3$@C	Sol–gel method	PVDF	SIB anode	84.5	2000	722	117
15	F-doped O3-type $NaNi_{1/3}Fe_{1/3}Mn_{1/3}O_2$	Solid-state reaction	NaF	SIB cathode	~110	70	150	120
16	F-doped $Na_3V_2(PO_4)_3$/C	Solid-state reaction	NaF	SIB cathode	97.8	1000	200	121
17	F-doped $Na_2VTi(PO_4)_3$	Sol–gel method	NH_4F	SIB cathode	~80	500	270	122
18	Cl-doped $LiFePO_4$/C	High-temperature solid phase method	NH_4Cl	LIB cathode	105.3	500	—	102
19	Br-doped $Li_4Ti_5O_{12}$	Solid-state reaction	LiBr	LIB anode	~122	300	—	103
20	Br-doped $Li_4Ti_5O_{12}$	CTAOH-assisted hydrothermal treatment	LiBr	LIB anode	106.2	1000	1750	104
21	S-doped graphene	Modified thermal process	—	SIB anode	217	1000	3200	118
22	N/P co-doped soft carbon	—	$(NH_4)_2HPO_4$	SIB anode	162	3000	1000	119

$_3Fe_{1/3}Mn_{1/3}O_{2-x}F_x$ ($x = 0$, 0.005, 0.01, 002, denoted as NFM-Fx) cathode materials for SIBs *via* a one-step solid-state reaction method. NFM-F0.01 exhibits the best cycling stability and rate performance, with a discharge capacity of ~110 mA h g^{-1} after the 70th cycle at a current density of 150 mA g^{-1} and a capacity retention rate of ~90%. The enhanced cycling stability is attributed to two effects: (i) F-doping regulates the oxygen binding energy and the Mn^{3+}/Mn^{4+} ratio, which can suppress the Jahn–Teller effect of Mn^{3+} and thus promote NFM-F electrochemical performance; (ii) F-doping allows a higher Na^+ diffusion rate and thus improves rate performance. As shown in Fig. 9e, the redox/oxidation peak of NFM-F0.01 was higher than that of NFM-F0, indicating that the polarization of NFM-F0.01 was lower, which means that the diffusion of Na^+ in NFM-F0.01 was higher than that in NFM-F0.[120]

Chen *et al.* synthesized an F-doped $Na_3V_2(PO_4)_{2.93}F_{0.07}$/C (F-0.07-NVP/C) composite as the cathode for SIBs by a solid-state reaction method. Compared to the undoped NVP/C sample, the F-0.07-NVP/C composite has a discharge capacity of 113 mA h g^{-1} at 10 mA g^{-1}, which is very close to the theoretical capacity (117 mA h g^{-1}). In terms of cycling performance, a reversible capacity of 97.8 mA h g^{-1} can be obtained and 86% of the capacity is maintained after 1000 cycles at 200 mA g^{-1}. F doping can inhibit the structural degradation of $Na_3V_2(PO_4)_3$ to $V_2(PO_4)_3$ and improve the structural stability (Fig. 9f). At the same time, it can reduce the particle size to decrease the pathway for Na^+ diffusion, thus effectively increasing the ionic conductivity.[121]

Song *et al.* synthesized F-doped $Na_{2-2x}VTi(PO_4)_{3-x}F_x$/C (denoted as NVTP-$F_x$, $x = 0.01$, 0.03 and 0.05) as cathodes for SIBs through a simple sol–gel method (Fig. 9g). Among the F-doped materials, the NVTP-$F_{0.03}$ electrode exhibits the best electrochemical performance. When the current density is increased from 0.1C to 10C, the specific capacity decreases from 134.3 to 75.4 m A h g^{-1}, and even when the applied current density is increased to 20C, a specific discharge capacity of 59.5 mA h g^{-1} is provided, which is much higher than that of the original sample. In addition, the NVTP-$F_{0.03}$ sample exhibits excellent cycling stability. After 100 cycles at 0.5C a capacity retention of 96.5% was achieved, and after 500 cycles at higher currents (2C) a capacity retention of 81.3% was still achieved. The results of the electrical analysis showed that the Na^+ diffusion kinetics were greatly improved after fluorine doping and that the carbon coating effectively facilitated charge transfer at the electrode.[122]

In order to better demonstrate the synthesis and application of F-doped materials/other element-doped materials in electrode materials, the preparation methods and cell performance are summarised in Table 3.

4 Conclusions

This paper reviews the progress of research on the synthesis of F-doped materials and their applications in batteries and catalysts. In recent years, F has gained a lot of attention in the field of materials as a cheap and efficient dopant. F-doping has been applied by researchers in photocatalysis, electrocatalysis, and rechargeable batteries. Firstly, F as a dopant in photocatalytic degradation of organic matter can inhibit photogenerated electron/hole recombination, increase the amount of –OH on the surface of the photocatalyst and increase the concentration of free electrons, and also make the particle size smaller, increase the specific surface area of the catalyst and improve the photocatalyst activity. Secondly, the introduction of F in electrocatalysis can change the electronic structure of the electrocatalyst and lower the reaction energy potential barrier, while increasing the electrical conductivity and improving the electrocatalytic selectivity and Faraday efficiency. Finally, doping F in the positive and negative electrode materials of LIBs and SIBs can improve the electronic conductivity of the materials, reduce the electrode polarisation, stabilize the crystal structure and accelerate the diffusion rate of lithium or sodium ions, thus improving the electrochemical performance of the batteries.

It is worth noting that, despite the good progress made in these areas with F-doped materials, their future development still faces challenges. F-doping is actually a relatively common topic in materials research, as it can alter the physical and chemical properties of materials and has important implications for a number of applications such as photocatalysts, electrocatalysts, and anode and cathode materials for rechargeable batteries, *etc.* However, the following may be among the reasons for the relative paucity of research on F doping: firstly, F doping is not possible for all materials and only some specific materials can be effectively doped with F ions. Therefore, this may limit the application and research of F doping in some materials. Secondly, the preparation method of F-doping is complicated and the amount of F ions doped is difficult to control, which makes the experimental study of F-doping difficult and requires more effort and time to optimise the preparation process. Thirdly, the doping of F ions in the material may affect the stability of the material, which may limit the use of F doping in some applications. Therefore, when conducting F-doping studies, the stability of the material needs to be fully considered, which adds to the difficulty of the study. Finally, there may be relatively few theoretical studies of F-doping compared to experimental studies, and this may be one of the reasons for the relative paucity of F-doping studies. Theoretical studies can be done to investigate the effect of F-doping on material properties through computational simulations and other methods, providing a theoretical basis and guidance for experimental studies.

F-doping has many potential applications, such as enhancing the optical, electrical and magnetic properties of materials and improving the performance of semiconductor devices. The following are the development prospects and research trends in F-doping: for example, F doping can be used to improve the performance of semiconductor materials, such as increasing the electrical conductivity of the material, reducing the particle size, increasing the specific surface area of the material, *etc.* F doping can also be used to develop new types of semiconductor materials, such as fluoride semiconductor materials, which have high electrical and optical properties and can be used in infrared detectors, laser diodes, *etc.* F doping is used to develop new types of catalysts, for example, doping F

into titanium dioxide catalysts can improve their catalytic performance and stability. F doping can also be used to improve the performance of rechargeable batteries, accelerate ion conduction rates, stabilise the structure of anode and cathode materials and extend battery life.

In other words, F-doped materials have excellent and unique physicochemical properties and have promising applications in catalysis and energy. We believe that in the future, with the joint efforts of researchers, F-doped materials will receive more attention and be widely used in more fields, showing the uniqueness of F-doped materials.

Conflicts of interest

There are no conflicts to declare.

Acknowledgements

This work was supported by the National Natural Science Foundation of China (61904123, 51973157) and the Tianjin Technical and Engineering Center of Nonwovens and State Key Laboratory of Membrane and Membrane Separation, Tiangong University (KF202103).

References

1 X. Jin, L. Ye, H. Xie and G. Chen, *Coord. Chem. Rev.*, 2017, **349**, 84–101.
2 S. R. Mishra and M. Ahmaruzzaman, *Nanoscale*, 2022, **14**, 1566–1605.
3 J. Sun, X. Li, Y. Quan, Y. Yin and S. Zheng, *Chemosphere*, 2015, **136**, 181–189.
4 J. Wen, X. Li, W. Liu, Y. Fang, J. Xie and Y. Xu, *Chin. J. Catal.*, 2015, **36**, 2049–2070.
5 S. Zhu and D. Wang, *Adv. Energy Mater.*, 2017, **7**, 1700841.
6 M. Moradi, Y. Vasseghian, A. Khataee, M. Harati and H. Arfaeinia, *Sep. Purif. Technol.*, 2021, **261**, 118274.
7 O. G. Sas, P. B. Sánchez, B. González and Á. Domínguez, *Sep. Purif. Technol.*, 2020, **236**, 116310.
8 W. Raza, J. Lee, N. Raza, Y. Luo, K.-H. Kim and J. Yang, *J. Ind. Eng. Chem.*, 2019, **71**, 1–18.
9 T. D. Vo, C. Lin, C. E. Weng, C. S. Yuan, C. W. Lee, C. H. Hung, X. T. Bui, K. C. Lo and J. X. Lin, *J. Environ. Manage.*, 2018, **217**, 327–336.
10 Q. Wang, B. Rhimi, H. Wang and C. Wang, *Appl. Surf. Sci.*, 2020, **530**, 147286.
11 R. Xie, D. Lei, Y. Zhan, B. Liu, C. H. A. Tsang, Y. Zeng, K. Li, D. Y. Leung and H. Huang, *Chem. Eng. J.*, 2020, **386**, 121025.
12 T. Bao, L. Song and S. Zhang, *Appl. Organomet. Chem.*, 2018, **32**, e4349.
13 H. Koyuncu and A. R. Kul, *Appl. Water Sci.*, 2020, **10**, 1–14.
14 S. Parakala, S. Moulik and S. Sridhar, *Chem. Eng. J.*, 2019, **375**, 122015.
15 A. A. Al-Gheethi, Q. M. Azhar, P. Senthil Kumar, A. A. Yusuf, A. K. Al-Buriahi, R. M. S. Radin Mohamed and M. M. Al-Shaibani, *Chemosphere*, 2022, **287**, 132080.
16 S. A. Bhat, N. Rashid, M. A. Rather, S. A. Bhat, P. P. Ingole and M. A. Bhat, *Chem. Phys. Lett.*, 2020, **754**, 137724.
17 P. Sathishkumar, R. A. A. Meena, T. Palanisami, V. Ashokkumar, T. Palvannan and F. L. Gu, *Sci. Total Environ.*, 2020, **698**, 134057.
18 B. M. Sharma, J. Becanova, M. Scheringer, A. Sharma, G. K. Bharat, P. G. Whitehead, J. Klanova and L. Nizzetto, *Sci. Total Environ.*, 2019, **646**, 1459–1467.
19 Y. Li, L. Zhang, X. Liu and J. Ding, *Sci. Total Environ.*, 2019, **658**, 333–342.
20 K. Poonia, V. Hasija, P. Singh, A. A. Parwaz Khan, S. Thakur, V. K. Thakur, S. Mukherjee, T. Ahamad, S. M. Alshehri and P. Raizada, *J. Cleaner Prod.*, 2022, **367**, 133087.
21 A. Fareed, A. Hussain, M. Nawaz, M. Imran, Z. Ali and S. U. Haq, *Environ. Technol. Innovation*, 2021, **24**, 101840.
22 R. Chen, Y. Zhuang, Y. Yu and B. Shi, *Water Res.*, 2021, **190**, 116660.
23 S. Poothong, E. Papadopoulou, J. A. Padilla-Sanchez, C. Thomsen and L. S. Haug, *Environ. Int.*, 2020, **134**, 105244.
24 C. Sun, J. Yang, M. Xu, Y. Cui, W. Ren, J. Zhang, H. Zhao and B. Liang, *Chem. Eng. J.*, 2022, **427**, 131564.
25 B. Wu, H. Meng, D. M. Morales, F. Zeng, J. Zhu, B. Wang, M. Risch, Z. J. Xu and T. Petit, *Adv. Funct. Mater.*, 2022, **32**, 2204137.
26 F. Zhang, Y. Zhu, Q. Lin, L. Zhang, X. Zhang and H. Wang, *Energy Environ. Sci.*, 2021, **14**, 2954–3009.
27 Y. Yang, C. R. Peltier, R. Zeng, R. Schimmenti, Q. Li, X. Huang, Z. Yan, G. Potsi, R. Selhorst, X. Lu, W. Xu, M. Tader, A. V. Soudackov, H. Zhang, M. Krumov, E. Murray, P. Xu, J. Hitt, L. Xu, H. Y. Ko, B. G. Ernst, C. Bundschu, A. Luo, D. Markovich, M. Hu, C. He, H. Wang, J. Fang, R. A. DiStasio Jr, L. F. Kourkoutis, A. Singer, K. J. T. Noonan, L. Xiao, L. Zhuang, B. S. Pivovar, P. Zelenay, E. Herrero, J. M. Feliu, J. Suntivich, E. P. Giannelis, S. Hammes-Schiffer, T. Arias, M. Mavrikakis, T. E. Mallouk, J. D. Brock, D. A. Muller, F. J. DiSalvo, G. W. Coates and H. D. Abruna, *Chem. Rev.*, 2022, **122**, 6117–6321.
28 Z. W. Seh, J. Kibsgaard, C. F. Dickens, I. Chorkendorff, J. K. Norskov and T. F. Jaramillo, *Science*, 2017, **355**, eaad4998.
29 Y. Chen, G. Li, Y. Zeng, L. Yan, X. Wang, L. Yang, Q. Wu and Z. Hu, *Nano Res.*, 2022, **15**, 7896–7902.
30 W. Ni, Y. Xue, X. Zang, C. Li, H. Wang, Z. Yang and Y. M. Yan, *ACS Nano*, 2020, **14**, 2014–2023.
31 S.-G. Han, D.-D. Ma, S.-H. Zhou, K. Zhang, W.-B. Wei, Y. Du, X.-T. Wu, Q. Xu, R. Zou and Q.-L. Zhu, *Appl. Catal., B*, 2021, **283**, 119591.
32 Y. Liu, Q. Li, X. Guo, X. Kong, J. Ke, M. Chi, Q. Li, Z. Geng and J. Zeng, *Adv. Mater.*, 2020, **32**, e1907690.
33 X. Zhu, Z. Liu, H. Wang, R. Zhao, H. Chen, T. Wang, F. Wang, Y. Luo, Y. Wu and X. Sun, *Chem. Commun.*, 2019, **55**, 3987–3990.
34 Y. P. Liu, Y. B. Li, H. Zhang and K. Chu, *Inorg. Chem.*, 2019, **58**, 10424–10431.
35 D. Yuan, Z. Wei, P. Han, C. Yang, L. Huang, Z. Gu, Y. Ding, J. Ma and G. Zheng, *J. Mater. Chem. A*, 2019, **7**, 16979–16983.

36 B. Yang, C. Jiang, G. Yu, Q. Zhuo, S. Deng, J. Wu and H. Zhang, *J. Hazard. Mater.*, 2015, **299**, 417–424.
37 R. Zhang, M. Zhang, H. Yang, G. Li, S. Xing, M. Li, Y. Xu, Q. Zhang, S. Hu, H. Liao and Y. Cao, *Small Methods*, 2021, **5**, e2100612.
38 Y. Chang, J. Chen, J. Jia, X. Hu, H. Yang, M. Jia and Z. Wen, *Appl. Catal., B*, 2021, **284**, 119721.
39 J. Neumann, M. Petranikova, M. Meeus, J. D. Gamarra, R. Younesi, M. Winter and S. Nowak, *Adv. Energy Mater.*, 2022, **12**, 2102917.
40 C. F. J. Francis, I. L. Kyratzis and A. S. Best, *Adv. Mater.*, 2020, **32**, e1904205.
41 Z. Hu, Q. Liu, S. L. Chou and S. X. Dou, *Adv. Mater.*, 2017, **29**, 1700606.
42 V. Vaiano, M. Matarangolo, J. J. Murcia, H. Rojas, J. A. Navío and M. C. Hidalgo, *Appl. Catal., B*, 2018, **225**, 197–206.
43 N. Villota, J. M. Lomas and L. M. Camarero, *Ultrason. Sonochem.*, 2017, **39**, 439–445.
44 C. Yu, Q. Fan, Y. Xie, J. Chen, Q. Shu and J. C. Yu, *J. Hazard. Mater.*, 2012, **237–238**, 38–45.
45 N. Imanaka, T. Masui and K. Yasuda, *Chem. Lett.*, 2011, **40**, 780–785.
46 B. Belaissaoui, Y. Le Moullec and E. Favre, *Energy*, 2016, **95**, 291–302.
47 W. Yu, X. Liu, L. Pan, J. Li, J. Liu, J. Zhang, P. Li, C. Chen and Z. Sun, *Appl. Surf. Sci.*, 2014, **319**, 107–112.
48 H. Miao, G.-F. Huang, J.-H. Liu, B.-X. Zhou, A. Pan, W.-Q. Huang and G.-F. Huang, *Appl. Surf. Sci.*, 2016, **370**, 427–432.
49 L. Rueda-Salaya, A. Hernández-Ramírez, L. Hinojosa-Reyes, J. Guzmán-Mar, M. Villanueva-Rodríguez and E. Sánchez-Cervantes, *J. Photochem. Photobiol., A*, 2020, **391**, 112364.
50 G. Vitiello, G. Iervolino, C. Imparato, I. Rea, F. Borbone, L. De Stefano, A. Aronne and V. Vaiano, *Sci. Total Environ.*, 2021, **762**, 143066.
51 E. M. Samsudin, S. B. A. Hamid, J. C. Juan, W. J. Basirun, A. E. Kandjani and S. K. Bhargava, *Appl. Surf. Sci.*, 2016, **365**, 57–68.
52 Y. Kang, X. Wu and Q. Gao, *ACS Sustainable Chem. Eng.*, 2019, **7**, 4210–4219.
53 H. Yu, C. Chu and X. An, *Appl. Organomet. Chem.*, 2019, **33**, e4682.
54 Z. Chen, W. Chen, G. Liao, X. Li, J. Wang, Y. Tang and L. Li, *J. Hazard. Mater.*, 2022, **428**, 128222.
55 A. Phuruangrat, P. Dumrongrojthanath, B. Kuntalue, S. Thongtem and T. Thongtem, *Mater. Lett.*, 2017, **196**, 256–259.
56 G.-Y. Zhang, J.-J. Wang, X.-Q. Shen, J.-J. Wang, B.-Y. Wang and D.-Z. Gao, *Appl. Surf. Sci.*, 2019, **470**, 63–73.
57 J. Zai, F. Cao, N. Liang, K. Yu, Y. Tian, H. Sun and X. Qian, *J. Hazard. Mater.*, 2017, **321**, 464–472.
58 C. Liu, L. Zhang, R. Liu, Z. Gao, X. Yang, Z. Tu, F. Yang, Z. Ye, L. Cui, C. Xu and Y. Li, *J. Alloys Compd.*, 2016, **656**, 24–32.
59 W. Ding, X. Zhang, X. Liu, Q. Lu, M. Wei and Y. Pang, *J. Environ. Chem. Eng.*, 2021, **9**, 105985.
60 Y. Shen, J.-y. Hu, L. Lu, C. Zhu, Q.-l. Fang and S. Song, *J. Zhejiang Univ. Sci. A*, 2022, **23**, 988–997.
61 T. N. Do, C. You and J. Kim, *Energy Environ. Sci.*, 2022, **15**, 169–184.
62 N. Li, X. Z. Chen, W. J. Ong, D. R. MacFarlane, X. J. Zhao, A. K. Cheetham and C. H. Sun, *ACS Nano*, 2017, **11**, 10825–10833.
63 D. D. Zhu, J. L. Liu and S. Z. Qiao, *Adv. Mater.*, 2016, **28**, 3423–3452.
64 J. Gu, F. Heroguel, J. Luterbacher and X. Hu, *Angew. Chem., Int. Ed. Engl.*, 2018, **57**, 2943–2947.
65 T. Wu, M. M. Melander and K. Honkala, *ACS Catal.*, 2022, **12**, 2505–2512.
66 X. Li, Y. Tian, X. Wang, Y. Guo and K. Chu, *Sustainable Energy Fuels*, 2021, **5**, 4277–4283.
67 W. Cai, Y. Han, Y. Pan, X. Zhang, J. Xu, Y. Zhang, Y. Sun, S. Li, J. Lai and L. Wang, *J. Mater. Chem. A*, 2021, **9**, 13483–13489.
68 S. Zhao, X. Lu, L. Wang, J. Gale and R. Amal, *Adv. Mater.*, 2019, **31**, e1805367.
69 F. Wang, Y. p. Liu, H. Zhang and K. Chu, *ChemCatChem*, 2019, **11**, 1441–1447.
70 C. Zuo, L. Li, W. Chen and Z. Zhang, *Appl. Surf. Sci.*, 2021, **554**, 149546.
71 Y. Wang, G. I. Waterhouse, L. Shang and T. Zhang, *Adv. Energy Mater.*, 2020, **11**, 2003323.
72 K. Zhao, Y. Su, X. Quan, Y. Liu, S. Chen and H. Yu, *J. Catal.*, 2018, **357**, 118–126.
73 W. Wang, X. Lu, P. Su, Y. Li, J. Cai, Q. Zhang, M. Zhou and O. Arotiba, *Chemosphere*, 2020, **259**, 127423.
74 S. Zeng, S. Wang, H. Zhuang, B. Lu, C. Li, Y. Wang and G. Wang, *Electrochim. Acta*, 2022, **420**, 140460.
75 X. Zheng, X. Cao, Z. Sun, K. Zeng, J. Yan, P. Strasser, X. Chen, S. Sun and R. Yang, *Appl. Catal., B*, 2020, **272**, 118967.
76 Q. Yang, Y. Jia, F. Wei, L. Zhuang, D. Yang, J. Liu, X. Wang, S. Lin, P. Yuan and X. Yao, *Angew. Chem., Int. Ed. Engl.*, 2020, **59**, 6122–6127.
77 M. Nemiwal, V. Gosu, T. C. Zhang and D. Kumar, *Int. J. Hydrogen Energy*, 2021, **46**, 10216–10238.
78 R. Moradi and K. M. Groth, *Int. J. Hydrogen Energy*, 2019, **44**, 12254–12269.
79 H. Zou, W. Rong, B. Long, Y. Ji and L. Duan, *ACS Catal.*, 2019, **9**, 10649–10655.
80 H. Luo, X. Wang, C. Wan, L. Xie, M. Song and P. Qian, *Nanomaterials*, 2022, **12**, 1081.
81 J. Li, Y. Zhang, X. Zhang, J. Huang, J. Han, Z. Zhang, X. Han, P. Xu and B. Song, *ACS Appl. Mater. Interfaces*, 2017, **9**, 398–405.
82 X. Ji, B. Liu, X. Ren, X. Shi, A. M. Asiri and X. Sun, *ACS Sustainable Chem. Eng.*, 2018, **6**, 4499–4503.
83 M. Li, B. Zhang, T. Cheng, S. Yu, S. Louisia, C. Chen, S. Chen, S. Cestellos-Blanco, W. A. Goddard and P. Yang, *Nano Res.*, 2021, **14**, 3509–3513.
84 J. Li, Y. Cai, H. Wu, Z. Yu, X. Yan, Q. Zhang, T. Z. Gao, K. Liu, X. Jia and Z. Bao, *Adv. Energy Mater.*, 2021, **11**, 2003239.

85 T. Weigel, F. Schipper, E. M. Erickson, F. A. Susai, B. Markovsky and D. Aurbach, *ACS Energy Lett.*, 2019, **4**, 508–516.
86 C. Yang, X. Ou, X. Xiong, F. Zheng, R. Hu, Y. Chen, M. Liu and K. Huang, *Energy Environ. Sci.*, 2017, **10**, 107–113.
87 G. Li, S. Cao, L. Fu, S. Wan and Q. Liu, *Electrochim. Acta*, 2021, **386**, 138470.
88 M. Cabello, E. Gucciardi, A. Herran, D. Carriazo, A. Villaverde and T. Rojo, *Molecules*, 2020, **25**, 2494.
89 H. Wang, Q. Pan, Q. Wu, X. Zhang, Y. Huang, A. Lushington, Q. Li and X. Sun, *J. Mater. Chem. A*, 2017, **5**, 4576–4582.
90 X. Bai, W. Li, A. Wei, Q. Chang, L. Zhang and Z. Liu, *Solid State Ionics*, 2018, **324**, 13–19.
91 X. Liu, G. Li, D. Zhang, L. Meng, B. Li and L. Li, *Electrochim. Acta*, 2020, **354**, 136655.
92 Y. Feng, C. Bai, K. Wu, H. Dong, J. Ke, X. Huang, D. Xiong and M. He, *J. Alloys Compd.*, 2020, **843**, 156085.
93 R. Jin, R. Li and H. Xu, *Ceram. Int.*, 2021, **47**, 24625–24631.
94 S. Zhu, B. Liang, X. Mou, X. Liang, H. Huang, D. Huang, W. Zhou, S. Xu and J. Guo, *J. Alloys Compd.*, 2022, **905**, 164142.
95 Q. Zhao, P. Peng, P. Zhu, G. Yang, X. Sun, R. Ding, P. Gao and E. Liu, *New J. Chem.*, 2022, **46**, 9612–9617.
96 J. H. Song, A. Kapylou, H. S. Choi, B. Y. Yu, E. Matulevich and S. H. Kang, *J. Power Sources*, 2016, **313**, 65–72.
97 C. Gao, J. Zhou, G. Liu and L. Wang, *J. Alloys Compd.*, 2017, **727**, 501–513.
98 C. Wang, Y. Xu, X. Sun, B. Zhang, Y. Chen and S. He, *J. Power Sources*, 2018, **378**, 345–352.
99 S. Choi, M.-C. Kim, S.-H. Moon, H. Kim and K.-W. Park, *Electrochim. Acta*, 2019, **326**, 135015.
100 J. Wang, C. Liu, G. Xu, C. Miao, M. Wen, M. Xu, C. Wang and W. Xiao, *Chem. Eng. J.*, 2022, **438**, 135537.
101 S.-B. Kim, H. Kim, D.-H. Park, J.-H. Kim, J.-H. Shin, J.-S. Jang, S.-H. Moon, J.-H. Choi and K.-W. Park, *J. Power Sources*, 2021, **506**, 230219.
102 H. Liu, S.-h. Luo, S.-x. Yan, Y.-f. Wang, Q. Wang, M.-q. Li and Y.-h. Zhang, *J. Electroanal. Chem.*, 2019, **850**, 113434.
103 J. B. Kim, S. G. Lee, S.-Y. Choi, J. Kim and S. O. Kim, *Ceram. Int.*, 2019, **45**, 17574–17579.
104 J. Wang, S. Zhao, J. Xie, D. Ruan and F. Zhao, *J. Solid State Chem.*, 2021, **303**, 122479.
105 W. Weng, J. Xu, C. Lai, Z. Xu, Y. Du, J. Lin and X. Zhou, *J. Alloys Compd.*, 2020, **817**, 152732.
106 Q. Deng, F. Zheng, W. Zhong, Q. Pan, Y. Liu, Y. Li, G. Chen, Y. Li, C. Yang and M. Liu, *Chem. Eng. J.*, 2020, **392**, 123735.
107 P. K. Nayak, L. Yang, W. Brehm and P. Adelhelm, *Angew. Chem., Int. Ed. Engl.*, 2018, **57**, 102–120.
108 Z. Y. Gu, J. Z. Guo, X. X. Zhao, X. T. Wang, D. Xie, Z. H. Sun, C. D. Zhao, H. J. Liang, W. H. Li and X. L. Wu, *InfoMat*, 2021, **3**, 694–704.
109 Z. Zhang, Y. Du, Q. C. Wang, J. Xu, Y. N. Zhou, J. Bao, J. Shen and X. Zhou, *Angew. Chem., Int. Ed. Engl.*, 2020, **59**, 17504–17510.
110 G. Zheng, Q. Lin, J. Ma, J. Zhang, Y. B. He, X. Tang, F. Kang, W. Lv and Q. H. Yang, *InfoMat*, 2021, **3**, 1445–1454.
111 Z. Yan, Q.-W. Yang, Q. Wang and J. Ma, *Chin. Chem. Lett.*, 2020, **31**, 583–588.
112 M. Wu, W. Ni, J. Hu and J. Ma, *Nano-Micro Lett.*, 2019, **11**, 44.
113 M. Song, C. Wang, D. Du, F. Li and J. Chen, *Sci. China: Chem.*, 2019, **62**, 616–621.
114 Y. Qi, W. Gao, H. Wang, D. Liu, J. Deng, B. Guo, S. Bao and M. Xu, *Chem. Eng. J.*, 2020, **402**, 126118.
115 Z. Chen, L. Lu, Y. Gao, Q. Zhang, C. Zhang, C. Sun and X. Chen, *Materials*, 2018, **11**, 2206.
116 P. Wei, Y. Liu, Y. Su, L. Miao, Y. Huang, Y. Liu, Y. Qiu, Y. Li, X. Zhang, Y. Xu, X. Sun, C. Fang, Q. Li, J. Han and Y. Huang, *ACS Appl. Mater. Interfaces*, 2019, **11**, 3116–3124.
117 Q. Deng, Q. Cheng, X. Liu, C. Chen, Q. Huang, J. Li, W. Zhong, Y. Li, J. Hu, H. Wang, L. Wu and C. Yang, *Chem. Eng. J.*, 2022, **430**, 132710.
118 B. Quan, A. Jin, S. H. Yu, S. M. Kang, J. Jeong, H. D. Abruna, L. Jin, Y. Piao and Y. E. Sung, *Adv. Sci.*, 2018, **5**, 1700880.
119 Y. Zhao, Y. Cong, H. Ning, X. Fei, C. Wu, H. Wang, Z. He, Y. Wang, Q. Zhao and M. Wu, *J. Alloys Compd.*, 2022, **918**, 165691.
120 Q. Zhang, Y. Huang, Y. Liu, S. Sun, K. Wang, Y. Li, X. Li, J. Han and Y. Huang, *Sci. China Mater.*, 2017, **60**, 629–636.
121 Y. Chen, Y. Xu, X. Sun, B. Zhang, S. He, L. Li and C. Wang, *J. Power Sources*, 2018, **378**, 423–432.
122 K. Song, Y. Zhu, Y. Jiang, X. Wang, J. Ma, C. Dai and L. Zhao, *J. Electroanal. Chem.*, 2021, **900**, 115597.